Impact of Scattering on the Capacity, Diversity, and Propagation Range of Multiple-Antenna Channels*

Ada S. Y. Poon†, David N. C. Tse‡, and Robert W. Brodersen§

1st January 2005

Abstract

Previous work on multiple-antenna channels uses the discrete-array model and captures the scattering condition of channel by introducing certain structures on the correlation across different antenna pairs. Performance results then depend on the characteristics of antenna arrays and the connection of the correlation structure to the physical scattering mechanisms is unclear. This paper uses a continuous-array model and introduces a two-step approach to model the scattering condition in an array-independent but manageable description of physical environments. The first step defines the spatial signal space that gives a compact view of the scattering channel. The second step applies wave scattering theory to model the underlying scattering mechanisms. Based on these modeling strategies, a more fundamental understanding of scattering channels is obtained, in particular, its impact on the spatial multiplexing gain, the diversity gain, as well as the trade-offs among spatial multiplexing, diversity, and propagation range. Insights obtained then guide the development of a transceiver architecture for the channel estimation of multiple-antenna systems that would utilize channel scattering more efficiently.

*Submitted to IEEE Trans. on Inform. Theory, April 2004; revised December 2004. The work of A. S. Y. Poon was support by the C2S2 of the Microelectronics Advanced Research Corporation (MARCO), DARPA, and the industrial members of Berkeley Wireless Research Center (BWRC), and was performed while she was at the BWRC, Department of Electrical Engineering and Computer Sciences, University of California at Berkeley. The material in this paper was presented in part at the Asilomar Conference on Signals, Systems and Computers, Pacific Grove, CA, December 2002.

†A. S. Y. Poon is with the Corporate Technology Group, Intel Corporation, Santa Clara, CA 95052 USA (e-mail: ada.y.poon@intel.com).

‡D. N. C. Tse is with the Department of Electrical Engineering and Computer Sciences, University of California at Berkeley, Berkeley, CA 94704 USA (e-mail: dtse@eecs.berkeley.edu).

§R. W. Brodersen is with the Berkeley Wireless Research Center, Department of Electrical Engineering and Computer Sciences, University of California at Berkeley, Berkeley, CA 94704 USA (e-mail: rb@eecs.berkeley.edu).

1 Introduction

Multiple-antenna systems improve performance dramatically by exploiting the scattering nature of physical environments. To better utilize this channel resource, [1–11] incorporate physical parameters of scattering condition into the channel model and study their effects on performances. While these results provide us with more practical insight, they are not sufficient to understand the fundamental limit of scattering channels. One major inadequacy of these approaches is the use of the correlation across different pairs of antennas to capture the scattering condition. By imposing different structures on this antenna correlation, the impact of channel scattering is concluded. While this antenna correlation depends on the scattering condition, it also depends on the location of antennas and therefore different array configurations will yield different conclusions even in the *same* channel.

To obtain more fundamental understanding of scattering channels, we use a *continuous-array model* which eliminates the need to specify *a priori* the number of antennas and their relative locations on the antenna array. [12] uses similar approach to model the antenna arrays. However, it uses the ray-tracing approach to model the scattering condition which lessens its analytical tractability. Instead, we apply wave scattering theory along with observations from channel measurements to model the scattering condition. Our approach is different from the mainstream analytical approach using discrete antenna arrays where the distribution of scatterers is modeled. For example, [1, 3, 9] consider the scatterer distribution being isotropic around the transmitter and/or the receiver – the ideal fully-scattered channel. However, channel measurements reveal that physical paths are more appropriately analyzed as clusters [13–16], as illustrated in Fig. 1. [4] therefore considers the scatterer distribution being clustered around several angular intervals. The complexity of the model, however, complicates the performance results where numerical examples are used to concluded the impact of scattering on performances.

In this paper, we introduce a two-step approach to model the scattering condition of physical environments. The first step takes into account the clustering phenomenon observed from channel measurements. The angular intervals subtended by scattering clusters, Θ_t and Θ_r (see Fig. 1), define the spatial signal space to interpret the scattering channel. From which we obtain a set of basis functions that gives the most compact view of the channel. [17] shows that the dimension of this set determines the available number of spatial degrees of freedom (spatial channels) given an area limitation on the transmit and receive antenna arrays[1]. The second step captures the connectivity between Θ_t and Θ_r introduced by the underlying scattering mechanism. We will consider the most basic scattering mechanisms: reflection, refraction, diffuse scattering, and diffraction. This modeling step allows us to compute various performance metrics. Then, we will divide the analyses into three

[1] [17] studies the effect of array geometry and polarization as well.

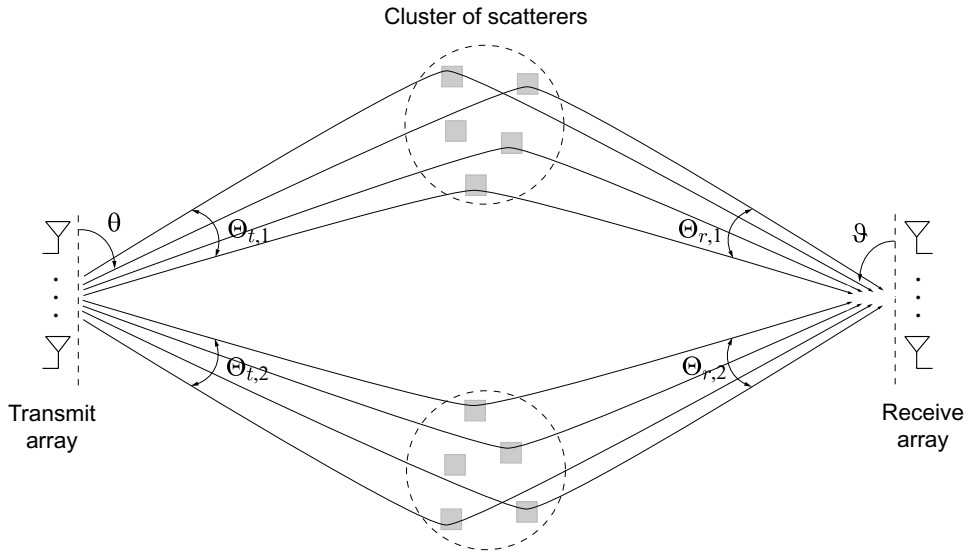

Figure 1: Illustrates the clustering of transmit and receive signals along the elevation direction and angles subtended by the scattering clusters as observed from the transmitter $\Theta_t = \Theta_{t,1} \cup \Theta_{t,2} \cup \cdots$ and from the receiver $\Theta_r = \Theta_{r,1} \cup \Theta_{r,2} \cup \cdots$.

regions according to the size of antenna arrays:

- When antenna arrays are small, the optimal radiation and reception patterns are omnidirectional. Power transfer becomes the major concern. The underlying scattering mechanisms critically determine the power gain with specular reflection being the most efficient while multi-bounce diffuse scattering being the least (see Fig. 2). For a given scattering mechanisms, the larger the widths of Θ_t and Θ_r are, the better is the receive SNR but their effect is secondary.

- When antenna arrays are large, the widths of Θ_t and Θ_r become critical as they determine the dimension of the basis to view the scattering channel. The ergodic capacity for linear arrays is shown to be[2]

$$C = L_t|\Omega_t| \log_2(\gamma \mathsf{SNR_t}) + o(L_t|\Omega_t|)$$

  at high SNR where L_t is the length of the transmit array normalized to a wavelength, $|\Omega_t| := \int_{\Theta_t} \sin\theta \, d\theta$, and $\mathsf{SNR_t}$ is the transmit SNR. The underlying scattering mechanisms determine the power gain per spatial channel denoted by γ and now become

[2]The expression assumes that the length of transmit array equals to that of the receive array and the width of Θ_t with respect to the axis of the transmit array equals to the width of Θ_r with respect to the axis of the receive array.

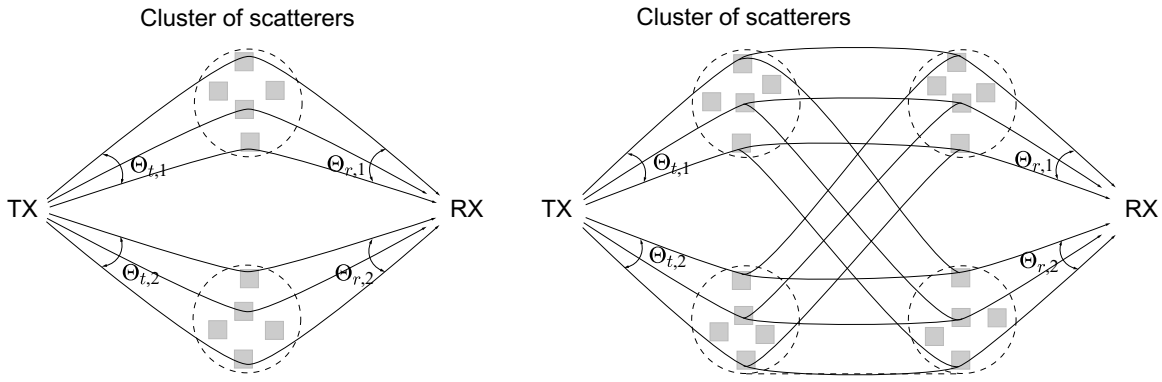

Figure 2: Illustrates (left) single-bounce diffuse scattering and (right) multi-bounce diffuse scattering.

a secondary effect. However, these mechanisms have critical impact on the diversity benefit. In particular, we will show that the single-bounce diffuse scattering and multi-bounce diffuse scattering (see Fig. 2) give very different trade-offs between spatial multiplexing gain (data rate) and diversity gain. Since real channels are more specular and single-bounce diffuse in nature, the insight obtained will help us design better space-time coding schemes. In addition, we will investigate the trade-off between propagation range and multiplexing gain such that a more comprehensive conclusion on the range-multiplexing-diversity trade-off can be drawn.

- When the size of antenna arrays is in between the above two limits, the number of spatial degrees of freedom is perplexing. It depends not only on the widths of Θ_t and Θ_r but also on the number of scattering clusters, angular positions of these clusters, and the SNR. We will illustrate that at high SNR, a higher throughput is supported by packing more antennas beyond the well-established half-wavelength antenna spacing criterion [18]. In terms of diversity benefits, the impact of different scattering mechanisms is not as distinguishable as when the antenna arrays are large. The distinction diminishes as antenna arrays become smaller but magnifies as antenna arrays become larger.

Finally, the proposed two-step approach to understand scattering channels leads the development of a two-stage transceiver architecture for channel estimation of multiple-antenna systems. The proposed architecture would make use of the channel resource due to the scattering nature of physical environment more effective and efficient.

The rest of the paper is organized as follows. Section 2 presents the continuous multiple-antenna channel model and the steps taken to simplify the model to make it analytically tractable. Section 3 introduces the spatial signal space to interpret the scattering channel.

Section 4 to 6 present performance analyses in the small-array regime, large-array regime, and finite-array regime respectively. Section 7 proposes a two-stage transceiver architecture for channel estimation. Finally, we will conclude this paper in Section 8.

In this paper, the following notation will be used. We use boldface capital letters for matrices and boldface small letter for vectors. For a vector $\mathbf{v}$, $\hat{\mathbf{v}}$ is a unit vector denoting its direction. $\mathbf{I}$ is the identity matrix. The determinant of a square matrix $\mathbf{A}$ is denoted by $\det(\mathbf{A})$ and its trace by $\mathrm{tr}(\mathbf{A})$. Two matrices related by $\mathbf{A} \succ \mathbf{B}$ implies that $\mathbf{A} - \mathbf{B}$ is positive definite. $\mathcal{C}^n$ and $\mathcal{C}^{n\times m}$ denote the set of n-dimensional complex vectors and $n \times m$ complex matrices respectively. $(\cdot)^*$, $(\cdot)^\dagger$ and $\mathsf{E}[\cdot]$ denote the conjugate, conjugate-transpose and expectation operations respectively. For an uncountable set $\mathcal{S}$, $|\mathcal{S}|$ denotes its Lebesgue measure. $\mathcal{CN}(\mu, \sigma^2)$ denotes a complex Gaussian random variable with mean μ and variance σ^2, and $\mathcal{CN}(\mathbf{M}, \mathbf{C} \otimes \mathbf{D})$ denotes a complex Gaussian random matrix with mean $\mathbf{M}$ and covariance $\mathbf{C} \otimes \mathbf{D}$ where $\otimes$ is the kronecker product. Two random variables related by $x \sim y$ means that they are statistically the same. $\lceil x \rceil$ gives the smallest integer equal to or greater than x.

2 System Model

We will first review the transmission in free-space in Section 2.1. Insights obtained will help deriving the continuous multiple-antenna channel model detailed in Section 2.2. Simplications will be introduced in Section 2.3 to make the model tractable for subsequent analyses.

2.1 Preliminaries

In line-of-sight channels, the receive power P_r is related to the transmit power P_t by the Friis transmission formula of classic antenna theory [18]

$$\frac{P_r}{P_t} = \frac{\mathcal{A}_r \mathcal{A}_t}{\lambda_c^2 l^2} \tag{1}$$

where $\mathcal{A}_t$ and $\mathcal{A}_r$ are the effective aperture of the transmit and receive antennas respectively, λ_c is the carrier wavelength, and l is the transmitter-receiver separation (propagation range). With reference to Fig. 3, the power gain can be expressed as a ratio of

$$\frac{P_r}{P_t} = \frac{|\Omega_t|}{\Delta\omega_t} \tag{2}$$

where

$$|\Omega_t| = \frac{\mathcal{A}_r}{l^2} \quad \text{and} \quad \Delta\omega_t := \frac{1}{\mathcal{A}_t/\lambda_c^2} \tag{3}$$

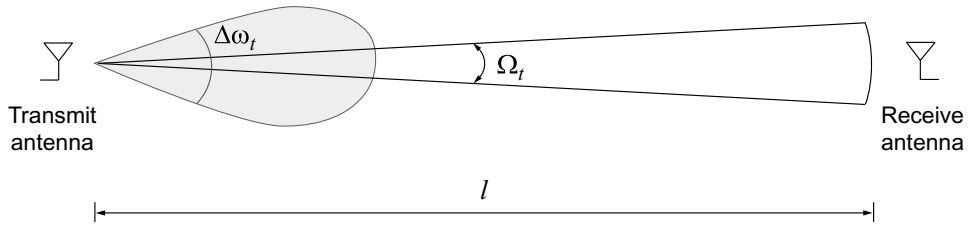

Figure 3: Illustrates the power gain of line-of-sight channels as a ratio of channel angular bandwidth $|\Omega_t|$ to transceiver angular resolvability $\Delta\omega_t$.

The $|\Omega_t|$ is the solid angle subtended by the receive antenna as seen from the transmitter. Only signals radiated within Ω_t are captured by the receiver and $|\Omega_t|$ is its measure. We therefore coin $|\Omega_t|$ the *channel angular bandwidth*. The $\Delta\omega_t$ is the beam-width of the transmit antenna and determines the *angular resolvability* of the transmit antenna over Ω_t.

In scattering environments, scatterers provide additional connectivities between the transmitter and the receiver. Equivalently, $|\Omega_t|$ is increased. However, this does not guarantee an increase in the power gain which also depends on the *underlying scattering mechanisms* and the electromagnetic properties of scatterers. The log-distance path loss model [19], a classical propagation model used to estimate the received signal strength as a function of l, states:

$$\frac{P_r}{P_t} = \frac{\mathcal{A}_r \mathcal{A}_t}{\lambda_c^2 l^n} \tag{4}$$

The path loss exponent n abstracts the impact of scattering on the power gain. In the line-of-sight channel, n equals 2. When the scattering is specular reflection, n is around 2. It can be less than 2 [20, 21] when scattering sources are lossless or the channel is unobstructed. In this case, the increase in the channel angular bandwidth $|\Omega_t|$ will increase the power gain. Now, when the scattering is diffuse or diffraction, n is around $2(\nu + 1)$ and ν is the number of scattering (bouncing) encountered by physical paths before reaching the receiver. That is, the power gain decreases despite of an increase in $|\Omega_t|$. Let us give an intuitive explanation. Consider a single-bounce diffuse channel ($n \approx 4$) where there is a single scatterer of effective cross-sectional area $\mathcal{A}_s$ located in the midway between the transmitter and the receiver. Defining $\delta := \log_l(4\mathcal{A}_s/\pi)$ and with reference to Fig. 4, the power gain can be expressed as a product of two ratios:

$$\frac{P_r}{P_t} = \frac{\mathcal{A}_r \mathcal{A}_t}{\lambda_c^2 l^{4-\delta}} = \frac{|\Omega_t|}{\Delta\omega_t} \cdot \frac{|\Omega_s|}{4\pi} \tag{5}$$

where

$$|\Omega_t| = \frac{\mathcal{A}_s}{(l/2)^2} \quad \text{and} \quad |\Omega_s| = \frac{\mathcal{A}_r}{(l/2)^2} \tag{6}$$

The fraction of power captured by the scatterer is $|\Omega_t|/\Delta\omega_t$ where only $|\Omega_s|/(4\pi)$ of the captured power reaches the receive antenna. Compared with (2), the single-bounce diffuse

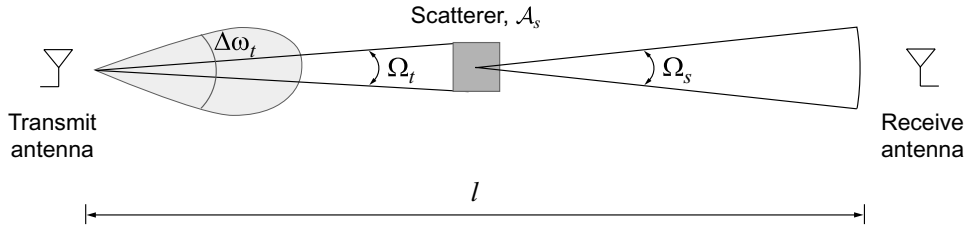

Figure 4: Illustrates the power gain of a single-bounce diffuse channel as a product of two ratios.

channel has an extra scaling factor of $|\Omega_s|/(4\pi)$. In general, each bounce encountered by physical paths introduces an extra scaling factor on the power gain and each of these factors is inversely proportional to l^2.

In summary, the path-loss model has three key parameters:

- angular resolvability of transceiver, $\Delta\omega_t$;
- angular bandwidth of channel, $|\Omega_t|$; and
- underlying scattering mechanisms: specular reflection versus diffuse scattering and single-bounce versus multi-bounce diffuse scattering.

These parameters not only impact the power gain but also the performance of multiple-antenna channels. To understand their impact, we will next introduce a spatial channel model that captures these three parameters while maintains *analytical tractability*.

2.2 Continuous Multiple-Antenna Channel Model

We consider continuous arrays which are composed of an infinite number of antennas separated by infinitesimal distances. This eliminates the need to specify *a priori* the number of antennas and their relative positions on antenna arrays. Each antenna is composed of three orthogonal dipoles oriented along Euclidean directions $\hat{\mathbf{e}}_1$, $\hat{\mathbf{e}}_2$ and $\hat{\mathbf{e}}_3$. In a frequency non-selective fading channel, the transmit and receive signals at a particular time are related by

$$\mathbf{y}(\mathbf{q}) = \int \mathbf{C}(\mathbf{q},\mathbf{p})\,\mathbf{x}(\mathbf{p})\,d\mathbf{p} + \mathbf{z}(\mathbf{q}) \tag{7}$$

The transmit signal $\mathbf{x}(\cdot)$ is a vector field on $\mathcal{R}^3$, a function that assigns each point $\mathbf{p} \in \mathcal{R}^3$ of the transmit array to a vector $\mathbf{x}(\mathbf{p}) \in \mathcal{C}^3$. Similarly, $\mathbf{y}(\cdot)$ is the receive vector field. The *channel response* $\mathbf{C}(\cdot,\cdot)$ is a 3×3 complex integral kernel where its domain is the set of transmit vector fields and its range is the set of receive vector fields. The matrix $\mathbf{C}(\mathbf{q},\mathbf{p})$ gives the channel gain and polarization between the transmit position $\mathbf{p}$ and receive position $\mathbf{q}$. The vector field $\mathbf{z}(\cdot)$ is the additive noise.

The channel response is a composition of five responses:

$$\mathbf{C}(\mathbf{q},\mathbf{p}) = \iint \mathbf{E}_r^{\dagger}(\hat{\boldsymbol{\kappa}},\mathbf{q})\,\mathbf{A}_r^{\dagger}(\hat{\boldsymbol{\kappa}},\mathbf{q})\,\mathbf{H}(\hat{\boldsymbol{\kappa}},\hat{\mathbf{k}})\,\mathbf{A}_t(\hat{\mathbf{k}},\mathbf{p})\,\mathbf{E}_t(\hat{\mathbf{k}},\mathbf{p})d\hat{\mathbf{k}}d\hat{\boldsymbol{\kappa}} \tag{8}$$

where $\mathbf{E}_t(\cdot,\cdot)$, $\mathbf{E}_r(\cdot,\cdot)$, $\mathbf{A}_t(\cdot,\cdot)$, $\mathbf{A}_r(\cdot,\cdot)$, and $\mathbf{H}(\cdot,\cdot)$ are 3×3 complex integral kernels, and are defined as follows:

- The *transmit element response* $\mathbf{E}_t(\cdot,\mathbf{p})$ gives the field pattern of the antenna element at $\mathbf{p}$. Similarly, $\mathbf{E}_r(\cdot,\cdot)$ is the *receive element response*. These element responses capture the mutual coupling between adjacent antenna elements, and between the antenna element and its surroundings. When there is no mutual coupling, $\mathbf{E}_t(\hat{\mathbf{k}},\mathbf{p})$ is independent of $\mathbf{p}$. Furthermore, if antenna elements are onmi-directional $\mathbf{E}_t(\hat{\mathbf{k}},\mathbf{p})$ is independent of both $\mathbf{p}$ and $\hat{\mathbf{k}}$.

- The *transmit array response* $\mathbf{A}_t(\hat{\mathbf{k}},\mathbf{p})$ maps the excitation current at $\mathbf{p}$ assuming onmi-directional element response to the radiated field along $\hat{\mathbf{k}}$. Similarly, the *receive array response* $\mathbf{A}_r(\cdot,\cdot)$ maps the incident field to the induced current distribution. In the far field, we can apply the plane wave approximation and obtain [17]

$$\mathbf{A}_t(\hat{\mathbf{k}},\mathbf{p}) = \left(\mathbf{I}-\hat{\mathbf{k}}\hat{\mathbf{k}}^{\dagger}\right)\exp(-j2\pi\hat{\mathbf{k}}^{\dagger}\mathbf{p}), \quad \mathbf{p}\in\mathcal{V}_t \tag{9a}$$

$$\mathbf{A}_r(\mathbf{q},\hat{\boldsymbol{\kappa}}) = \left(\mathbf{I}-\hat{\boldsymbol{\kappa}}\hat{\boldsymbol{\kappa}}^{\dagger}\right)\exp(-j2\pi\hat{\boldsymbol{\kappa}}^{\dagger}\mathbf{q}), \quad \mathbf{q}\in\mathcal{V}_r \tag{9b}$$

  where $\mathcal{V}_t$ and $\mathcal{V}_r$ denote the transmit and receive spaces respectively. In the expression, the position vectors $\mathbf{p}$ and $\mathbf{q}$ are normalized by the wavelength λ_c for conciseness.

- The *scattering response* $\mathbf{H}(\hat{\boldsymbol{\kappa}},\hat{\mathbf{k}})$ gives the channel gain and polarization between the transmit direction $\hat{\mathbf{k}}$ and the receive direction $\hat{\boldsymbol{\kappa}}$. [22] refers it the double-directional channel response and illustrates its properties by measurement results. Most spatial channel measurements reveal that scattered paths are typically clustered around a number of disjoint angular intervals (see Fig. 1). Therefore, $\mathbf{H}(\cdot,\cdot)$ is non-zero in multiple sub-intervals only. Suppose there are M_t scattering clusters illuminated by the transmit array with angular sub-intervals of $\Omega_{t,i}$ $(i=1,\cdots,M_t)$ and M_r clusters as observed from the receive array with sub-intervals of $\Omega_{r,i}$ $(i=1,\cdots,M_r)$. Then, the scattering response satisfies

$$\mathbf{H}(\hat{\boldsymbol{\kappa}},\hat{\mathbf{k}}) \neq 0 \quad \text{only if} \quad (\hat{\boldsymbol{\kappa}},\hat{\mathbf{k}}) \in \Omega_r \times \Omega_t \tag{10}$$

  where

$$\Omega_t = \bigcup_{i=1}^{M_t}\Omega_{t,i} \quad \text{and} \quad \Omega_r = \bigcup_{i=1}^{M_r}\Omega_{r,i}$$

Table 1: Examples of scattering sources and their underlying scattering mechanisms.

Mechanisms	Examples of scattering sources		
	3 kHz–300 MHz	300 MHz–3 GHz	$>$ 3 GHz
Reflection/Refraction	Ionosphere	Buildings	Walls
Diffuse Scattering	Troposphere	Plants	Furniture
Diffraction	Earth surface	Hills	Door-way openings

Now, $|\mathcal{V}_t|$ and $|\mathcal{V}_r|$ capture the angular resolvability of transceiver, and $|\Omega_t|$ and $|\Omega_r|$ capture the angular bandwidth of channel. We will next model $\mathbf{H}(\cdot,\cdot)$ within $\Omega_r \times \Omega_t$ to capture the underlying scattering mechanisms.

Specular Reflection

Starting with reflection, it occurs when the scattering source is smooth and large as compared to a wavelength, for example, the back-wall reflection (see Table 1). The incident and reflected directions make equal angles from the surface normal. Suppose $\hat{\mathbf{n}}$ is the unit normal of the surface (see Fig. 5). For an impulse applied in the direction $\hat{\mathbf{k}}$, the signal scattered in the direction $\hat{\boldsymbol{\kappa}}$ is

$$\mathbf{H}(\hat{\boldsymbol{\kappa}},\hat{\mathbf{k}}) = e^{-j2\pi r}\delta\big(\hat{\boldsymbol{\kappa}} - \boldsymbol{\Theta}(\hat{\mathbf{n}})\hat{\mathbf{k}}\big)\,\boldsymbol{\Gamma}_{SP}(\hat{\mathbf{n}}\times\hat{\mathbf{k}},\hat{\mathbf{k}}) \tag{11}$$

where

$$\begin{aligned}\boldsymbol{\Theta}(\hat{\mathbf{n}}) &= \mathbf{I} - 2\hat{\mathbf{n}}\hat{\mathbf{n}}^{\dagger}\\ \boldsymbol{\Gamma}_{SP}(\mathbf{v},\hat{\mathbf{k}}) &= \frac{\eta_2\sqrt{1-v^2}-\sqrt{\eta_1^2-\eta_2^2v^2}}{\eta_2\sqrt{1-v^2}+\sqrt{\eta_1^2-\eta_2^2v^2}}\,\hat{\mathbf{v}}\hat{\mathbf{v}}^{\dagger}\\ &\quad - \frac{\eta_1^2/\eta_2\sqrt{1-v^2}-\sqrt{\eta_1^2-\eta_2^2v^2}}{\eta_1^2/\eta_2\sqrt{1-v^2}+\sqrt{\eta_1^2-\eta_2^2v^2}}\,(\hat{\mathbf{v}}\times\hat{\mathbf{k}})(\hat{\mathbf{v}}\times\hat{\mathbf{k}})^{\dagger}\end{aligned}$$

v is the magnitude of $\mathbf{v}$, η_1 and η_2 are the intrinsic impedance of free space and the scattering source respectively, and r is the distance traveled normalized to the wavelength. The matrix $\boldsymbol{\Theta}(\hat{\mathbf{n}})$ determines the rotation on the propagation direction and $\boldsymbol{\Gamma}_{SP}(\hat{\mathbf{n}}\times\hat{\mathbf{k}},\hat{\mathbf{k}})$ determines the change in polarization.

Now, let us generalize it to the cluster response:

$$\mathbf{H}_{SP}(\hat{\boldsymbol{\kappa}},\hat{\mathbf{k}}) = e^{-j2\pi f_c\tau_i(\hat{\mathbf{k}})}\delta\big(\hat{\boldsymbol{\kappa}} - \boldsymbol{\Theta}(\hat{\mathbf{n}}_i)\hat{\mathbf{k}}\big)\,\boldsymbol{\Gamma}_{SP,i}(\hat{\mathbf{n}}_i\times\hat{\mathbf{k}},\hat{\mathbf{k}}),\quad \hat{\mathbf{k}}\in\Omega_{t,i},\ i=1,\cdots,M_t \tag{12}$$

where $\hat{\mathbf{n}}_i$ and $\boldsymbol{\Gamma}_{SP,i}$ are the unit normal and polarization matrix of the ith scattering cluster respectively, $\tau_i(\hat{\mathbf{k}})$ is the delay along $\hat{\mathbf{k}}\in\Omega_{t,i}$, and f_c is the carrier frequency. The response has two distinct features:

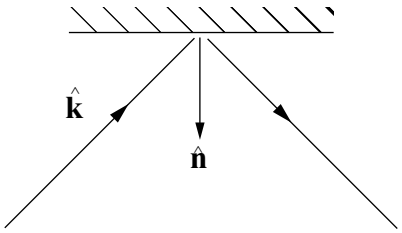

Figure 5: Illustrates specular reflection.

- the transmit direction $\hat{\mathbf{k}}$ and the receive direction $\hat{\boldsymbol{\kappa}}$ are in *one-to-one correspondence*; and
- the response is inherently *deterministic*.

Same conclusions are drawn for refraction.

Diffuse Scattering

Diffuse scattering occurs when the scattering source is composed of a volume of small discrete scatterers, small as compared to a wavelength (see Table 1 for some examples). Upon impinging, the incident fields induce electric and magnetic dipoles on each discrete scatterer. The induced dipoles then *re-radiate* energy in directions other than the incident direction (see Fig. 6). The scattering response for each individual discrete scatterer is [23][3]

$$\mathbf{H}(\hat{\boldsymbol{\kappa}}, \hat{\mathbf{k}}) = e^{-j2\pi r}\boldsymbol{\Gamma}_{SD}(\hat{\boldsymbol{\kappa}}, \hat{\mathbf{k}}) \tag{13}$$

where

$$\boldsymbol{\Gamma}_{SD}(\hat{\boldsymbol{\kappa}}, \hat{\mathbf{k}}) = \frac{\epsilon_r - 1}{\epsilon_r + 2}\left(\mathbf{I} - \hat{\mathbf{k}}\hat{\mathbf{k}}^{\dagger}\right) + \frac{\mu_r - 1}{\mu_r + 2}\left(\hat{\boldsymbol{\kappa}}\hat{\mathbf{k}}^{\dagger} - \hat{\boldsymbol{\kappa}}^{\dagger}\hat{\mathbf{k}}\mathbf{I}\right) \tag{14}$$

ϵ_r and μ_r are the relative permittivity and relative permeability of the scatterer respectively, and r is the distance traveled normalized to the wavelength. Compared to specular reflection, the transmit and receive directions are no longer in one-to-one correspondence. In other words, the transmit and receive directions are more connected. Summing together the contribution from each individual scatterer yields (see Fig. 7)

$$e^{-j2\pi r}\boldsymbol{\Gamma}_{SD}(\hat{\boldsymbol{\kappa}}, \hat{\mathbf{k}}) \cdot \frac{1}{\sqrt{N}} \sum_{n=1}^{N} e^{j\mathbf{k}_{eff}^{\dagger}\mathbf{r}_n}$$

where r is the distance traveled as measured from the centroid of the scattering volume, $\mathbf{r}_n$ is the position of the nth scatterer relative to the centroid, and $\mathbf{k}_{eff}$ is the effective wavenumber of the scattering volume. As the size of the scattering volume is typically

[3]The scattering process discussed is also known as Rayleigh scattering.

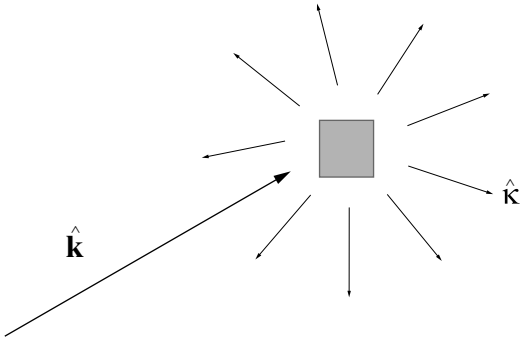

Figure 6: Illustrates diffuse scattering from a single scatterer.

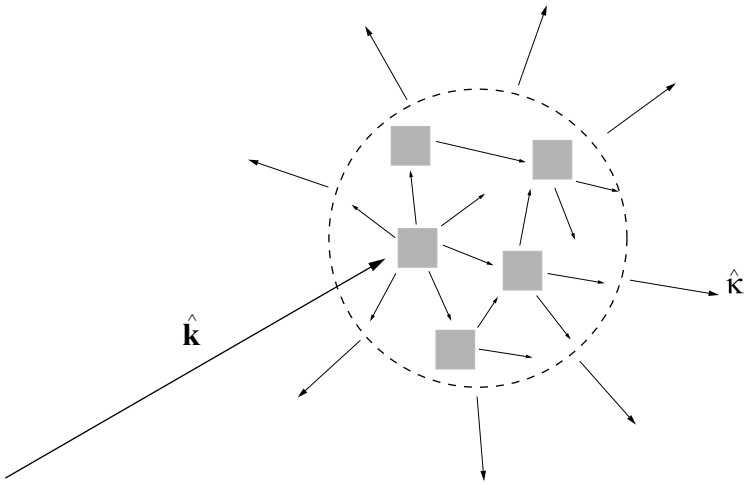

Figure 7: Illustrates diffuse scattering from a cluster of scatterers.

large as compared to a wavelength and the volume contains a lot of discrete scatterers, the displacement vector $\mathbf{r}_n$ can be modeled as a random variable in space and the phase lag $\mathbf{k}_{eff}^{\dagger}\mathbf{r}_n$ is approximately uniformly distributed in $[0, 2\pi)$. By the central limit theorem,

$$e^{-j2\pi r}\frac{1}{\sqrt{N}}\sum_{n=1}^{N} e^{j\mathbf{k}_{eff}^{\dagger}\mathbf{r}_n} \sim \mathcal{CN}(0,1)$$

As r and $\mathbf{k}_{eff}$ are functions of $\hat{\mathbf{k}}$ and $\hat{\boldsymbol{\kappa}}$, the single-bounce diffuse response is

$$\mathbf{H}_{SD}(\hat{\boldsymbol{\kappa}}, \hat{\mathbf{k}}) = w_i(\hat{\boldsymbol{\kappa}}, \hat{\mathbf{k}})\boldsymbol{\Gamma}_{SD,i}(\hat{\boldsymbol{\kappa}}, \hat{\mathbf{k}}), \quad (\hat{\boldsymbol{\kappa}}, \hat{\mathbf{k}}) \in \Omega_{r,i} \times \Omega_{t,i},\ i \in \{1, \cdots, M_t\} \tag{15}$$

where $w_i(\hat{\boldsymbol{\kappa}}, \hat{\mathbf{k}})$ is a complex Gaussian random process capturing the randomness of the ith scattering cluster.

Because of the secondary-source property of diffuse scattering, the multi-bounce diffuse response is a convolution of single-bounce diffuse responses:

$$\mathbf{H}_{MD}(\hat{\boldsymbol{\kappa}}, \hat{\mathbf{k}}) = \mathbf{W}_{ij}(\hat{\boldsymbol{\kappa}}, \hat{\mathbf{k}}), \quad (\hat{\boldsymbol{\kappa}}, \hat{\mathbf{k}}) \in \Omega_{r,i} \times \Omega_{t,j},\ (i,j) \in \{1, \cdots, M_r\} \times \{1, \cdots, M_t\} \quad (16)$$

where $\mathbf{W}(\cdot,\cdot)$'s are 3×3 complex random processes. For example, a double-bounce channel has

$$\mathbf{W}_{ij}(\hat{\boldsymbol{\kappa}}, \hat{\mathbf{k}}) = \int_{\Omega_{s,ij}} w_{ri}(\hat{\boldsymbol{\kappa}}, \hat{\mathbf{v}}) \boldsymbol{\Gamma}_{SD,ri}(\hat{\boldsymbol{\kappa}}, \hat{\mathbf{v}}) w_{tj}(\hat{\mathbf{v}}, \hat{\mathbf{k}}) \boldsymbol{\Gamma}_{SD,tj}(\hat{\mathbf{v}}, \hat{\mathbf{k}})\, d\hat{\mathbf{v}} \quad (17)$$

where $\Omega_{s,ij}$ is the angular interval subtended by the ith scattering cluster at the receive side as seen from the jth scattering cluster at the transmit side. The randomness of $\mathbf{W}_{ij}(\cdot,\cdot)$'s critically depends on the number of bouncing encountered by physical paths. Unlike the single-bounce response, the transmit and receive directions are now fully connected as illustrated in Fig. 2.

The single-bounce and multi-bounce diffuse responses have two distinct features:

- the transmit and receive directions are more connected; and
- the response is inherently *stochastic*.

In particular, the scattering source acts like a secondary source and functions like a *passive* relay.

Finally, diffraction occurs when the scattering source has sharp edges, for example, around door-way openings (see Table 1). Each point in the diffraction region generates a secondary field upon impinging by an incident field which is similar to diffuse scattering. Therefore, we consider diffuse scattering and diffraction as alike.

2.3 Simplified Model

The model presented so far captures the essence of the angular resolvability of transceiver, the angular bandwidth of channel, and the underlying scattering mechanisms. Next, we introduce five steps to simple the model and make it analytically tractable:

1. *Element responses.* We will not investigate the effect of mutual coupling. Thus, the element reponses becomes

$$\mathbf{E}_r(\hat{\boldsymbol{\kappa}}, \mathbf{q}) = \mathbf{E}_t(\hat{\mathbf{k}}, \mathbf{p}) = \frac{1}{4\pi}\mathbf{I}$$

2. *Array responses.* We consider linear arrays oriented along the z-axis. In spherical coordinates, the propagation directions can be expressed as

$$\hat{\mathbf{k}} = \begin{bmatrix} \sin\theta\cos\phi \\ \sin\theta\sin\phi \\ \cos\theta \end{bmatrix} \quad \text{and} \quad \hat{\boldsymbol{\kappa}} = \begin{bmatrix} \sin\vartheta\cos\varphi \\ \sin\vartheta\sin\varphi \\ \cos\vartheta \end{bmatrix}$$

The array responses can therefore be written as

$$\mathbf{A}_t(\hat{\mathbf{k}}, \mathbf{p}) = \big(\mathbf{I} - \hat{\mathbf{k}}\hat{\mathbf{k}}^\dagger\big) e^{-j2\pi p_z \cos\theta} \delta(p_x)\delta(p_y), \quad |p_z| \le \frac{L_t}{2}$$
$$\mathbf{A}_r(\mathbf{q}, \hat{\boldsymbol{\kappa}}) = \big(\mathbf{I} - \hat{\boldsymbol{\kappa}}\hat{\boldsymbol{\kappa}}^\dagger\big) e^{-j2\pi q_z \cos\vartheta} \delta(q_x)\delta(q_y), \quad |q_z| \le \frac{L_r}{2}$$

where L_t and L_r are the length of the transmit and receive arrays respectively.

3. *Scattering responses.* For specular reflection, $\|\boldsymbol{\Theta}(\hat{\mathbf{n}}_i)\|$ is unity for all $\hat{\mathbf{n}}_i$ implying $|d\hat{\boldsymbol{\kappa}}| = |d\hat{\mathbf{k}}|$, we therefore consider

$$\mathbf{H}_{SP}(\hat{\boldsymbol{\kappa}}, \hat{\mathbf{k}}) = e^{-j2\pi f_c \tau_i(\hat{\mathbf{k}})} \delta(\hat{\boldsymbol{\kappa}} - \hat{\mathbf{k}})\, \boldsymbol{\Gamma}_{SP,i}(\hat{\mathbf{n}}_i \times \hat{\mathbf{k}}, \hat{\mathbf{k}}), \quad \hat{\mathbf{k}} \in \Omega_{t,i},\ i = 1, \cdots, M_t \tag{18}$$

For the single-bounce diffuse scattering, we consider $w_i(\hat{\boldsymbol{\kappa}}, \hat{\mathbf{k}})$'s are uncorrelated, zero mean and unit variance white complex Gaussian random processes, that is,

$$\mathsf{E}\big[w_i(\hat{\boldsymbol{\kappa}}, \hat{\mathbf{k}}) w_{i'}^*(\hat{\boldsymbol{\kappa}}', \hat{\mathbf{k}}')\big] = \delta(\hat{\boldsymbol{\kappa}} - \hat{\boldsymbol{\kappa}}')\delta(\hat{\mathbf{k}} - \hat{\mathbf{k}}')\delta_{ii'}, \quad (\hat{\boldsymbol{\kappa}}, \hat{\mathbf{k}}) \in \Omega_{r,i} \times \Omega_{t,i} \tag{19}$$

Finally for the multi-bounce diffuse channel, we consider

$$\mathsf{E}\big[\mathbf{W}_{ij}(\hat{\boldsymbol{\kappa}}, \hat{\mathbf{k}}) \mathbf{W}_{i'j'}^\dagger(\hat{\boldsymbol{\kappa}}', \hat{\mathbf{k}}')\big] = \frac{1}{l^{2(\nu-1)}} \delta(\hat{\boldsymbol{\kappa}} - \hat{\boldsymbol{\kappa}}')\delta(\hat{\mathbf{k}} - \hat{\mathbf{k}}')\delta_{ii'}\delta_{jj'} \quad (\hat{\boldsymbol{\kappa}}, \hat{\mathbf{k}}) \in \Omega_{r,i} \times \Omega_{t,j} \tag{20}$$

where l is the transmitter-receiver separation and ν is the number of bouncing encountered by physical paths. As the multi-bounce response is a convolution of single-bounce responses, the normalization by $l^{2(\nu-1)}$ is due to the differential in the convolution as shown in (17) for the double-bounce response.

4. *Polarization.* The above simplication on the multi-bounce diffuse channel hardly true except when there are substantial number of bounces. But if we do not consider the role of polarization on performances and focus on scalar responses instead of matrix responses, the simplication is more justifiable. Now the channel response becomes

$$c(\mathbf{q}, \mathbf{p}) = \frac{1}{(4\pi)^2} \iint a_r^*(\hat{\boldsymbol{\kappa}}, \mathbf{q}) h(\hat{\boldsymbol{\kappa}}, \hat{\mathbf{k}}) a_t(\hat{\mathbf{k}}, \mathbf{p})\, d\hat{\mathbf{k}} d\hat{\boldsymbol{\kappa}} \tag{21}$$

in which the array responses are

$$a_t(\hat{\mathbf{k}}, \mathbf{p}) = e^{-j2\pi p_z \cos\theta} \delta(p_x)\delta(p_y), \quad |p_z| \le \frac{L_t}{2} \tag{22a}$$
$$a_r(\hat{\boldsymbol{\kappa}}, \mathbf{q}) = e^{-j2\pi q_z \cos\vartheta} \delta(q_x)\delta(q_y), \quad |q_z| \le \frac{L_r}{2} \tag{22b}$$

the specular response is

$$h_{SP}(\hat{\boldsymbol{\kappa}}, \hat{\mathbf{k}}) = e^{-j2\pi f_c \tau(\hat{\mathbf{k}})} \delta(\hat{\boldsymbol{\kappa}} - \hat{\mathbf{k}}), \quad \hat{\boldsymbol{\kappa}}, \hat{\mathbf{k}} \in \Omega_t = \Omega_r \tag{23}$$

and the diffuse responses satisfy

$$\mathsf{E}\big[h_{SD}(\hat{\boldsymbol{\kappa}},\hat{\mathbf{k}})h^*_{SD}(\hat{\boldsymbol{\kappa}}',\hat{\mathbf{k}}')\big] = \delta(\hat{\boldsymbol{\kappa}}-\hat{\boldsymbol{\kappa}}')\delta(\hat{\mathbf{k}}-\hat{\mathbf{k}}'), \quad (\hat{\boldsymbol{\kappa}},\hat{\mathbf{k}}) \in \bigcup_{i=1}^{M_t} \Omega_{r,i}\times\Omega_{t,i} \tag{24a}$$

$$\mathsf{E}\big[h_{MD}(\hat{\boldsymbol{\kappa}},\hat{\mathbf{k}})h^*_{MD}(\hat{\boldsymbol{\kappa}}',\hat{\mathbf{k}}')\big] = \frac{1}{l^{2(\nu-1)}}\delta(\hat{\boldsymbol{\kappa}}-\hat{\boldsymbol{\kappa}}')\delta(\hat{\mathbf{k}}-\hat{\mathbf{k}}'), \quad (\hat{\boldsymbol{\kappa}},\hat{\mathbf{k}}) \in \Omega_r\times\Omega_t \tag{24b}$$

where $\tau(\hat{\mathbf{k}}) = \tau_i(\hat{\mathbf{k}})$ for $i = 1,\cdots,M_t$. The single-bounce diffuse response $h_{SD}(\hat{\boldsymbol{\kappa}},\hat{\mathbf{k}})$ is a complex Gaussian random process. To simplify the model further, we limit subsequent analyses to $h_{MD}(\hat{\boldsymbol{\kappa}},\hat{\mathbf{k}})$ being a zero-mean complex Gaussian random process as well.

5. *Propagation directions.* As linear arrays can only resolve the elevation direction (θ or ϑ), further simplications yield

$$c(q_z,p_z) = \frac{1}{2^2}\iint a_r(\cos\vartheta,q_z)^* h(\cos\vartheta,\cos\theta)a_t(\cos\theta,p_z)\,\sin\theta\sin\vartheta\,d\theta d\vartheta \tag{25}$$

Now, $h(\cos\vartheta,\cos\theta)$ is non-zero only within $\Omega_{\theta,r}\times\Omega_{\theta,t}$ where $\Omega_{\theta,t} = \{\cos\theta : \theta\in\Theta_t\}$, $\Omega_{\theta,r} = \{\cos\vartheta : \vartheta\in\Theta_r\}$, and Θ_t and Θ_r are the angular intervals subtended by scattering clusters along the elevation direction of the transmitter and the receiver respectively (see Fig. 1).

To simplify the notation in subsequent analyses, we will drop the subscript θ on $\Omega_{\theta,t}$ and $\Omega_{\theta,r}$, z on p_z and q_z, and the factor $1/2^2$ from now on. Furthermore, we define $\alpha := \cos\theta$ and $\beta := \cos\vartheta$. The channel response then becomes

$$c(q,p) = \iint a_r^*(\beta,q)h(\beta,\alpha)a_t(\alpha,p)\,d\alpha d\beta \tag{26}$$

in which the array responses are

$$a_t(\alpha,p) = e^{-j2\pi\alpha}, \quad |p| \le \frac{L_t}{2} \quad \text{and} \quad a_r(\beta,q) = e^{-j2\pi\beta}, \quad |q| \le \frac{L_r}{2} \tag{27}$$

the specular response is

$$h_{SP}(\beta,\alpha) = e^{-j2\pi f_c\tau(\alpha)}\delta(\beta-\alpha), \quad \beta,\alpha\in\Omega_t=\Omega_r \tag{28}$$

and the diffuse responses satisfy

$$\mathsf{E}\big[h_{SD}(\beta,\alpha)h^*_{SD}(\beta',\alpha')\big] = \delta(\beta-\beta')\delta(\alpha-\alpha'), \quad (\beta,\alpha) \in \bigcup_{i=1}^{M_t} \Omega_{r,i}\times\Omega_{t,i} \tag{29a}$$

$$\mathsf{E}\big[h_{MD}(\beta,\alpha)h^*_{MD}(\beta',\alpha')\big] = \frac{1}{l^{\nu-1}}\delta(\beta-\beta')\delta(\alpha-\alpha'), \quad (\beta,\alpha) \in \Omega_r\times\Omega_t \tag{29b}$$

The normalization on the multi-bounce diffuse response is now $l^{\nu-1}$ instead of $l^{2(\nu-1)}$ because only one propagation direction is accounted for (the differential in the convolution changes from $d\hat{\mathbf{k}} = d\alpha\, d\phi$ to $d\alpha$.) Furthermore, $h_{SD}(\beta,\alpha)$ and $h_{MD}(\beta,\alpha)$ are zero-mean complex Gaussian random processes.

In general, the scattering response $h(\beta,\alpha)$ is a superposition of $h_{SP}(\beta,\alpha)$, $h_{SD}(\beta,\alpha)$, and $h_{MD}(\beta,\alpha)$. Those component responses have very different power gains (see Section 2.1). Depending on the physical environment and the carrier frequency, $h(\beta,\alpha)$ is usually dominated by one of them. Therefore, we will perform analyses on them individually. Next, we will give the set of basis functions that gives the most compact look of the scattering response.

3 Optimal Basis for $h(\beta,\alpha)$

The scattering response is sandwiched between two integral kernels:

$$a_t(\alpha,p), \quad (\alpha,p) \in \Omega_t \times [-L_t/2, L_t/2] \tag{30a}$$

$$a_r(\beta,q), \quad (\beta,q) \in \Omega_r \times [-L_r/2, L_r/2] \tag{30b}$$

As these kernels are non-zero and square integrable, there exist two sets of orthonormal functions $\{\eta_{t,m}(\alpha)\}$ and $\{\xi_{t,m}(p)\}$, and a sequence of positive numbers in a decreasing order $\{\sigma_{t,m}\}$ such that [24, Therorem 8.4.1]

$$a_t(\alpha,p), \quad (\alpha,p) \in \Omega_t \times [-L_t/2, L_t/2] = \sum_{m=1}^{\infty} \sigma_{t,m}\eta_{t,m}(\alpha)\xi_{t,m}(p) \tag{31}$$

The expansion is equivalent to the singular value decomposition on finite dimensional matrices and $\sigma_{t,m}$'s are the singular values. Similarly,

$$a_r(\beta,q), \quad (\beta,q) \in \Omega_r \times [-L_r/2, L_r/2] = \sum_{n=1}^{\infty} \sigma_{r,n}\eta_{r,n}(\beta)\xi_{r,n}(q) \tag{32}$$

Three points are noted:

- The behavior of $\sigma_{t,m}$ with m and that of $\sigma_{r,n}$ with n determine the number of spatial degrees of freedom. Fig. 8 plots the $\sigma_{t,m}^2$ for a channel with 3 scattering clusters each of angle 30°. It illustrates that there is a limit on the number of significant singular values. Suppose there are N_t significant $\sigma_{t,m}$ and N_r significant $\sigma_{r,n}$. Then, the minimum of N_t and N_r gives the number of spatial degrees of freedom [17]. In addition, we notice that the transition between good and bad singular values is more abrupt for large L_t. Therefore, we divide subsequent anlyses into three regions: small-array regime ($L_t|\Omega_t|, L_r|\Omega_r| \ll 1$), large-array regime ($L_t|\Omega_t|, L_r|\Omega_r| \gg 1$), and finite-array regime.

- The left eigenfunctions $\eta_{t,m}(\alpha)$ and $\eta_{r,n}(\beta)$ form the basis to project the scattering response. In particular, on knowing Ω_t at the transmitter and Ω_r at the receiver only, the subset

$$\left\{\eta^*_{r,n}(\beta)\eta_{t,m}(\alpha) : m = 1, \cdots, N_t, n = 1, \cdots, N_r\right\} \tag{33}$$

  is the optimal basis for the scattering response. Fig. 9 plots the eigenfunctions for the same channel and $L_t = 4$. These functions, as expected, are non-zero only in Θ_t. The $\eta_{t,1}(\alpha)$ has most energy in the middle sub-interval, $\eta_{t,2}(\alpha)$ in the first sub-interval, and $\eta_{t,4}(\alpha)$ in the third sub-interval, while $\eta_{t,3}$ is spread over the entire Θ_t.

- The right eigenfunctions $\xi_{t,m}(p)$ and $\xi_{r,n}(q)$ are the current distributions that yield the radiation and reception patterns with decreasing efficiency. It is because

$$\Xi_{t,m}(\alpha) := \int_{-L_t/2}^{L_t/2} a_t(\alpha, p)\xi_{t,m}(p)\, dp$$
$$\Xi_{r,n}(\beta) := \int_{-L_r/2}^{L_r/2} a_r(\beta, q)\xi_{r,n}(q)\, dq$$

  have $\sigma^2_{t,m}$ of the energy within Θ_t and $\sigma^2_{r,n}$ of the energy within Θ_r respectively. Therefore,

$$\left\{\Xi_{t,m}(\alpha) : m = 1, \cdots, N_t\right\} \quad \text{and} \quad \left\{\Xi_{r,n}(\beta) : n = 1, \cdots, N_r\right\} \tag{34}$$

  give the respective set of optimal radiation patterns and reception patterns. Fig. 10 plots the optimal radiation patterns for the same channel and antenna array. The $\Xi_{t,4}(\alpha)$ has most energy spilling out Θ_t while $\Xi_{t,1}(\alpha)$ has the least. These optimal sets are key to the design of an efficient mutliple-antenna transceiver detailed in Section 7.

Note that the basis introduced depends on both the scattering condition and the size of antenna arrays. The basis introduced in [7], however, is independent of the scattering condition. [7] uses sinc functions to approximate $\Xi_{t,m}(\alpha)$ and $\Xi_{r,n}(\beta)$ which is not well-justified for clustered channels as shown by the plots in Fig. 10.

Now, we can obtain a discrete representation for the input-output model in (7) by projecting the scattering response $h(\beta, \alpha)$, the input signal $x(p)$, the output signal $y(q)$, and the additive noise $z(q)$ onto the left and right eigenfunctions. Defining

$$H_{nm} := \iint \eta^*_{r,n}(\beta)h(\beta, \alpha)\eta_{t,m}(\alpha)\, d\alpha d\beta$$
$$x_m := \int x(p)\xi^*_{t,m}(p)\, dp$$
$$y_n := \int y(q)\xi^*_{r,n}(q)\, dq$$
$$z_n := \int z(q)\xi^*_{r,n}(q)\, dq$$

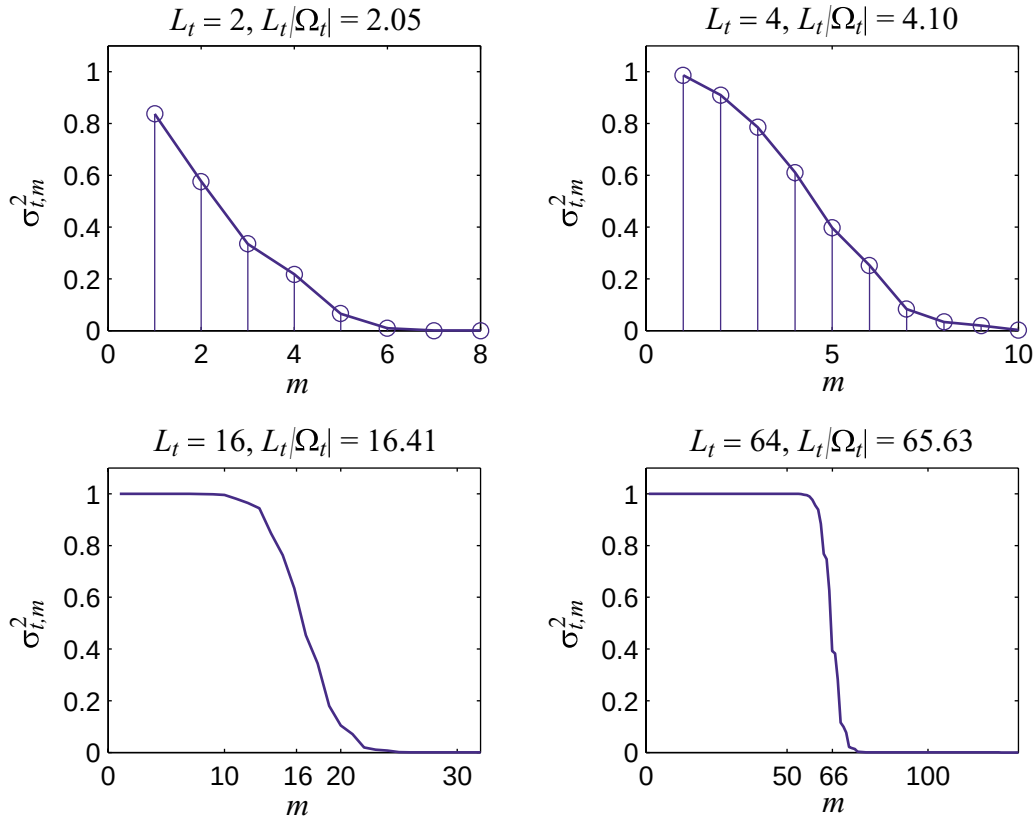

Figure 8: Plots $\sigma^2_{t,m}$ for $\Theta_t = [25°, 55°] \cup [80°, 110°] \cup [145°, 175°]$ ($|\Omega_t| = 1.0254$) and L varying from 2 to 64.

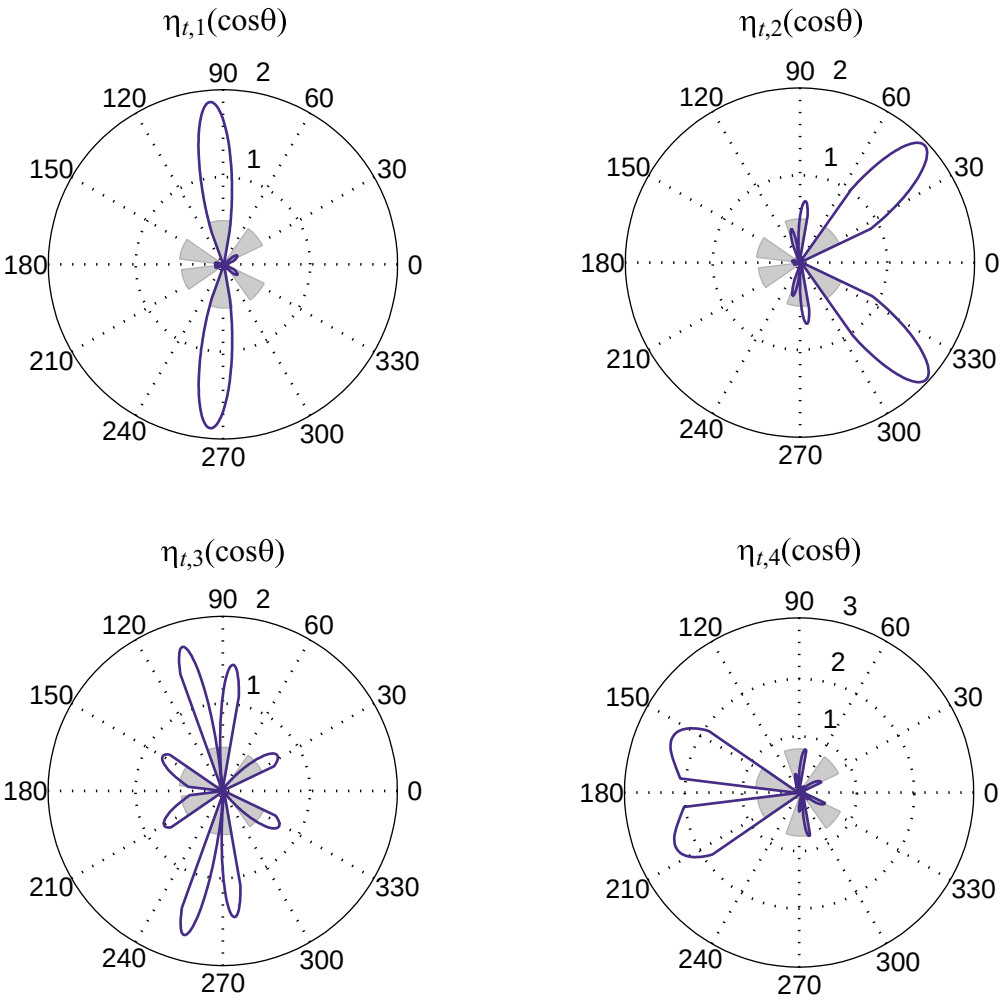

Figure 9: Plots $\eta_{t,n}(\cos\theta)$ for $\Theta_t = [25°, 55°] \cup [80°, 110°] \cup [145°, 175°]$ and $L_t = 4$. The subintervals in Θ_t is shaded. Note that $\int_0^\pi |\eta_{t,m}(\cos\theta)|^2 \sin\theta \, d\theta = 1$ and therefore, $\eta_{t,4}(\cos\theta)$ has magnitude larger than the others.

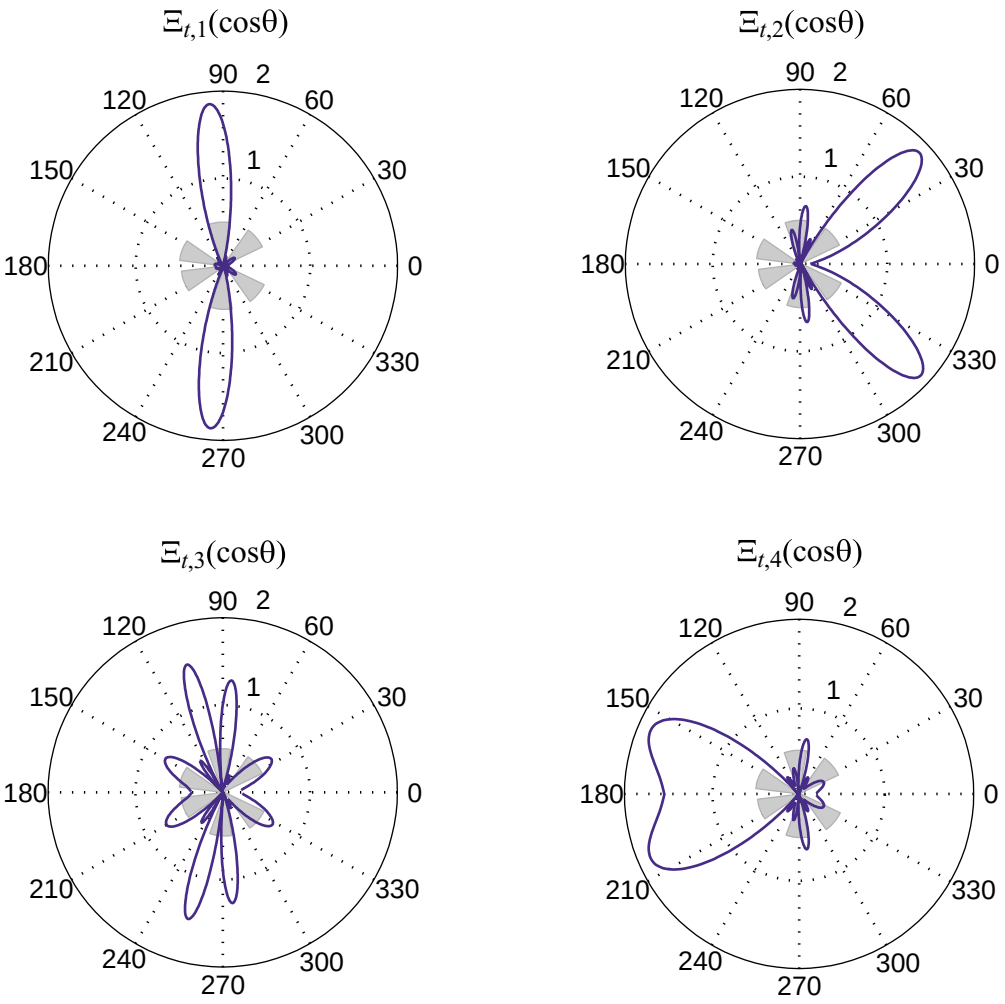

Figure 10: Plots $\Xi_{t,n}(\cos\theta)$ for $\Theta_t = [25°, 55°] \cup [80°, 110°] \cup [145°, 175°]$ and $L_t = 4$. The sub-intervals in Θ_t is shaded.

yields the discrete representation:

$$y_n = \sum_{m=1}^{\infty} \sigma_{r,n} H_{nm} \sigma_{t,m} x_m + z_n, \quad n \in \{1, 2, \cdots\} \tag{35}$$

In conclusion, the impact of scattering on multiple-antenna systems has two spatial scales:

- *Coarse-scale.* The Ω_t and Ω_r determine the behavior of $\sigma_{t,m}$ and $\sigma_{r,n}$, and hence determine the dimension of the channel matrix $\mathbf{H}$,

  $$\mathbf{H} := \left[H_{nm}\right]_{n=1,\cdots,N_r;\, m=1,\cdots,N_t}$$

  They also determine the set of basis functions for projecting the scattering response, and the set of optimal radiation and reception patterns for transceiver design.

- *Fine-scale.* The connectivity between the transmit and receive directions within $\Omega_r \times \Omega_t$ determines the well-conditionedness of $\mathbf{H}$. Thus, the underlying scattering mechanisms would affect the space-time coding scheme used.

In the following analyses, we will first derive the eigenvalue distributions and the basis functions for $h(\beta, \alpha)$ in each regime of operation. Then, we will obtain a matrix form of the response $\mathbf{H}$ for each scattering mechanism. Based on which we develop the main results that distinguish the impact of coarse-scale and that of fine-scale scattering on performances. The insight obtained leads to a two-stage transceiver design for multiple-antenna systems.

4 Small-Array Regime

The small-array regime refers to: $L_t|\Omega_t| \ll 1$ and $L_r|\Omega_r| \ll 1$. In this regime, there are only one significant $\sigma_{t,m}$ and one significant $\sigma_{r,n}$ so the channel is simple. We will introduce the tool to study the trade-offs among spatial multiplexing, diversity, and propagation range.

4.1 Main Results

As $L_t|\Omega_t|, L_r|\Omega_r| \ll 1$, we have the following decomposition:

$$a_t(\alpha, p) = e^{-j2\pi p\alpha}, \quad (\alpha, p) \in \Omega_t \times [-L_t/2, L_t/2] \tag{36a}$$

$$\approx 1, \quad (\alpha, p) \in \Omega_t \times [-L_t/2, L_t/2] \tag{36b}$$

$$= \sqrt{L_t|\Omega_t|} \cdot \frac{1}{\sqrt{|\Omega_t|}} \chi_{\Omega_t}(\alpha) \cdot \frac{1}{\sqrt{L_t}} \Pi(\frac{p}{L_t}) \tag{36c}$$

where

$$\Pi(p) := \begin{cases} 1, & |p| \le 1/2 \\ 0, & \text{otherwise} \end{cases} \quad \text{and} \quad \chi_{\Omega}(\alpha) := \begin{cases} 1, & \alpha \in \Omega \\ 0, & \text{otherwise} \end{cases}$$

There is only one significant singular value $\sigma_{t,1} = \sqrt{L_t|\Omega_t|}$ and the corresponding eigenfunctions are: $\eta_{t,1}(\alpha) = \frac{1}{\sqrt{|\Omega_t|}}\chi_{\Omega_t}(\alpha)$ and $\xi_{t,1}(p) = \frac{1}{\sqrt{L_t}}\Pi(\frac{p}{L_t})$. The optimal radiation pattern is omni-directional. Similarly,

$$a_r(\beta, q) \approx \sqrt{L_r|\Omega_r|} \cdot \frac{1}{\sqrt{|\Omega_r|}}\chi_{\Omega_r}(\alpha) \cdot \frac{1}{\sqrt{L_r}}\Pi(\frac{p}{L_r}) \tag{37}$$

Now, we project the scattering response corresponding to different scattering mechanisms onto $\eta^*_{r,1}(\beta)\eta_{t,1}(\alpha)$ and obtain:

- *Specular channels.* The channel matrix is given by

$$H_{11} = \frac{1}{|\Omega_t|}\int_{\Omega_t} e^{-j2\pi f_c \tau(\alpha)}\, d\alpha \tag{38a}$$

$$\overset{(a)}{\sim} \frac{1}{|\Omega_t|}\,\mathcal{CN}(0, |\Omega_t|) \tag{38b}$$

$$\sim \frac{1}{\sqrt{|\Omega_t|}}\,\mathcal{CN}(0, 1) \tag{38c}$$

  As f_c is typically large, the phase lag, $2\pi f_c \tau(\alpha)$, is approximately uniformly distributed over $[0, 2\pi)$. By the central limit theorem, (a) holds. The receive SNR is related to the transmit SNR by

$$\frac{\mathsf{SNR_r}}{\mathsf{SNR_t}} = \sigma^2_{t,1}\sigma^2_{r,1}\,\mathsf{E}\big[|H_{11}|^2\big] = L_t L_r|\Omega_t| \tag{39}$$

- *Multi-bounce diffuse channels.* The channel matrix is

$$H_{11} = \iint \eta^*_{r,1}(\beta)h_{MD}(\beta,\alpha)\eta_{t,1}(\alpha)\, d\alpha d\beta \tag{40a}$$

$$\overset{(a)}{\sim} \frac{1}{l^{(\nu-1)/2}}\int_{\Omega_r}\int_{\Omega_t} \eta^*_{r,1}(\beta)h_w(\beta,\alpha)\eta_{t,1}(\alpha)\, d\alpha d\beta \tag{40b}$$

$$\overset{(b)}{\sim} \frac{1}{l^{(\nu-1)/2}}\iint \eta^*_{r,1}(\beta)h_w(\beta,\alpha)\eta_{t,1}(\alpha)\, d\alpha d\beta \tag{40c}$$

$$\overset{(c)}{\sim} \frac{1}{l^{(\nu-1)/2}}\,\mathcal{CN}(0, 1) \tag{40d}$$

  where $h_w(\beta, \alpha)$ is a zero-mean unit-variance white complex Gaussian random process over all β and α. As $h_{MD}(\beta, \alpha)$ is a zero-mean white complex Gaussian random process over $\Omega_r \times \Omega_t$, (a) holds. As illustrated by Fig. 9, $\eta_{r,n}(\cdot)$ and $\eta_{t,m}(\cdot)$ are non-zero only over Ω_r and Ω_t respectively so (b) holds. (c) is due to the circularly symmetric property of $h_w(\beta, \alpha)$. The ratio of receive SNR to transmit SNR is therefore

$$\frac{\mathsf{SNR_r}}{\mathsf{SNR_t}} = \frac{1}{l^{\nu-1}}\, L_t L_r|\Omega_t||\Omega_r| \tag{41}$$

- *Single-bounce diffuse channels.* The channel matrix is

$$H_{11} \overset{(a)}{=} \frac{1}{\sqrt{|\Omega_t||\Omega_r|}} \sum_{i=1}^{M_t} \int_{\Omega_{r,i}} \int_{\Omega_{t,i}} h_{SD}(\beta,\alpha)\, d\alpha d\beta \tag{42a}$$

$$\overset{(b)}{\sim} \frac{1}{\sqrt{|\Omega_t||\Omega_r|}} \sum_{i=1}^{M_t} \mathcal{CN}\big(|\Omega_{r,i}||\Omega_{t,i}|\big) \tag{42b}$$

$$\sim \sqrt{\sum_{i=1}^{M_t} \frac{|\Omega_{r,i}|}{|\Omega_r|}\frac{|\Omega_{t,i}|}{|\Omega_t|}}\, \mathcal{CN}(0,1) \tag{42c}$$

(a) is from the property of $\eta_{t,1}(\alpha)$ and $\eta_{r,1}(\beta)$ while (b) is from the property of $h_{SP}(\beta,\alpha)$. The ratio of receive SNR to transmit SNR is

$$\frac{\mathsf{SNR_r}}{\mathsf{SNR_t}} = L_t L_r \sum_{i=1}^{M_t} |\Omega_{t,i}||\Omega_{r,i}| \tag{43}$$

If $|\Omega_{t,i}|$'s and $|\Omega_{r,i}|$'s are individually the same, the ratio will be

$$\frac{\mathsf{SNR_r}}{\mathsf{SNR_t}} = \frac{1}{M_t} L_t L_r |\Omega_t||\Omega_r|$$

4.2 Power Gain and its Trade-offs with Propagation Range

In Section 2.1, the channel angular bandwidth in both line-of-sight channel and single-scatterer single-bounce diffuse channel are inversely proportional to $1/l^2$ (see (3) and (6)). In clustered channels, will this relationship remain held? Cast to our simplified model where only elevation direction is considered due to the use of linear arrays, we will investigate if the following is true at least to the first order:

$$|\Omega_t|, |\Omega_r| \propto \frac{1}{l} \tag{44}$$

If the scattering clusters remain fixed while the transmitter-receiver separation is changing, this relationship will obviously maintain. However, in general changing the transmitter-receiver separation will bring in or fade out scattering clusters. For example, Fig. 11 shows a physical environment where scattering clusters are located in the midway between the transmitter and the receiver with $b > a$ where a is the diameter of the cluster and b is the cluster-cluster separation. The transmit and receive channel angular bandwidth are both equal to

$$|\Omega_t| = |\Omega_r| = \frac{4a}{l} \sum_{n=0}^{\infty} \frac{1}{1+(2n+1)^2(b/l)^2} \tag{45}$$

It is bounded by

$$\frac{\pi a}{bl}\big(1 - \frac{2}{\pi}\tan^{-1}\frac{b}{l}\big) \le |\Omega_t| = |\Omega_r| \le \frac{\pi a}{bl}\big(1 + \frac{2}{\pi}\tan^{-1}\frac{b}{l}\big) \tag{46}$$

implying

$$|\Omega_t| = |\Omega_r| = \frac{\pi a}{b}\frac{1}{l} + o(1/l) \tag{47}$$

for large l. Therefore, we draw the following hypothesis on the channel angular bandwidth:

Hypothesis 4.1. *At propagation range of l, the transmit and receive channel angular bandwidth of linear arrays satisfy*

$$|\Omega_t| = \frac{|\Omega_{t0}|}{l} \quad \textit{and} \quad |\Omega_r| = \frac{|\Omega_{r0}|}{l} \tag{48}$$

where $|\Omega_{t0}|$ and $|\Omega_{r0}|$ are the respective transmit and receive channel angular bandwidth at the reference range $l_0 = 1m$.

Now, the power gain of specular, multi-bounce diffuse, and single-bounce diffuse channels can be written as

$$\begin{aligned} g_{SP}(l) &= L_t L_r |\Omega_t| &&= \frac{L_t L_r}{l^{1-\delta_{SP}}} \\ g_{MD}(l) &= \frac{1}{l^{\nu-1}} L_t L_r |\Omega_t||\Omega_r| &&= \frac{L_t L_r}{l^{\nu+1-\delta_{MD}}} \\ g_{SD}(l) &= \frac{1}{M_t} L_t L_r |\Omega_t||\Omega_r| &&= \frac{L_t L_r}{l^{2-\delta_{SD}}} \end{aligned}$$

respectively, where $\delta_{SP} = \log_l |\Omega_{t0}|$, $\delta_{MD} = \log_l(|\Omega_{t0}||\Omega_{r0}|)$, and $\delta_{SD} = \log_l(|\Omega_{t0}||\Omega_{r0}|/M_t)$. Three main points are concluded:

- The results are consistent with the path loss model in (1) and therefore reinforce Hypothesis 4.1. Later in Section 5.5, we will apply this hypothesis to bring out the trade-off between spatial degrees of freedom and propagation range.
- Not surprisingly there is a trade-off between power gain and propagation range, and this trade-off varies with the underlying scattering mechanism as illustrated in Fig. 12.
- For a particular scattering mechanism and a fixed propagation range, there are three contributing components: the transmit beamforming gain (L_t), the receive beamforming gain (L_r), and the scattering gain (δ_{SP}, δ_{MD}, or δ_{SD}). The length of the transmit array determines how well the transmitter can focus its energy to a particular direction: the larger it is, the more the transmit power can be focused on the direction of scattering sources. These scattering sources then relay the transmit power to the receiver. Therefore, the larger the angular bandwidth is, the more the transmit power can reach the receiver. At the receiver, the length of the receive array determines the amount of additive noise and interfering signals captured together with the desired signal. The larger the receive array is, the better its noise immunity is.

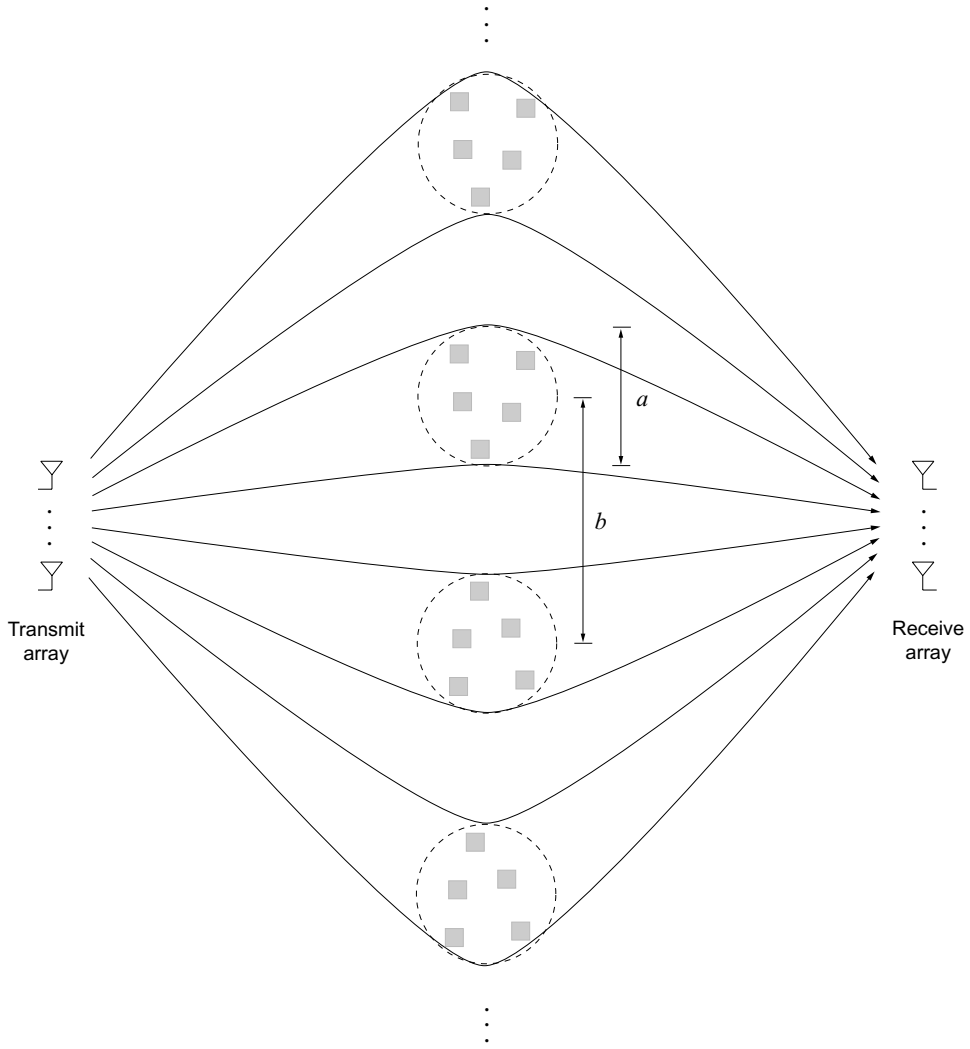

Figure 11: A physical environment with an infinite line of scattering clusters in the midway between the transmitter and the receiver.

4.3 Multiplexing-Diversity Trade-offs

Not a coincidence, the three scattering mechanisms yield the same scalar Rayleigh fading channel with different variances. The impact of scattering on the diversity gain is thus straightforward. At a fixed target rate, the outage probability decays like $\mathsf{SNR_r}^{-1}$ at high SNR. The diversity gain is therefore unity and is insensitive to the underlying scattering mechanisms. Increasing the target rate R (bits/s/Hz) reduces this decay. For example, consider uncoded communication using QAM. The minimum Euclidean distance is approximately

$$d_{\min}^2 \approx \frac{\mathsf{SNR_r}}{2^R}$$

and the error probability at high SNR is approximately

$$P_e \approx \mathsf{E}_{\chi^2}\left[Q\Big(\sqrt{\frac{\chi^2 d_{\min}^2}{2}}\Big)\right] \approx (d_{\min}^2)^{-1} \approx 2^R\,\mathsf{SNR_r}^{-1} = \mathsf{SNR_r}^{-(1-\frac{R}{\log \mathsf{SNR_r}})}$$

where χ^2 has a chi-square distribution with 2 degrees of freedom. If the target rate increases with SNR, the diversity gain will become $1 - R/\log \mathsf{SNR_r}$. The maximum diversity gain is unity. To capture this trade-off between data rate and error probability, we use the trade-off formulation proposed in [25].

Definition 4.2. *A diversity gain $d(r)$ is achieved at multiplexing gain r if the data rate is*

$$R = r \log \mathsf{SNR_r},$$

and the outage probability is

$$P_{out}(R) \approx \mathsf{SNR_r}^{-d(r)}$$

or more precisely,

$$\lim_{\mathsf{SNR_r}\to\infty} \frac{\log P_{out}(r \log \mathsf{SNR_r})}{\log \mathsf{SNR_r}} = -d(r)$$

The curve $d(r)$ characterizes the multiplexing-diversity trade-off of the channel.

The specular, multi-bounce diffuse and single-bounce diffuse channels have the same outage probability:

$$P_{out} = P\big(\log(1+\chi^2\mathsf{SNR_r}) < r\log \mathsf{SNR_r}\big) = P\Big(\chi^2 < \frac{\mathsf{SNR_r}^r - 1}{\mathsf{SNR_r}}\Big) \overset{(a)}{\approx} \mathsf{SNR_r}^{-(1-r)}$$

at high SNR. For small ϵ, $P(\chi^2 < \epsilon) \approx \epsilon$ and therefore (a) holds. From which, we obtain the trade-off curves

$$d_{SP}(r) = d_{MD}(r) = d_{SD}(r) = 1 - r \tag{49}$$

Fig. 12 plots these trade-off curves. Unlike the trade-offs between power gain and propagation range, the trade-offs between multiplexing and diversity gains are the same for all

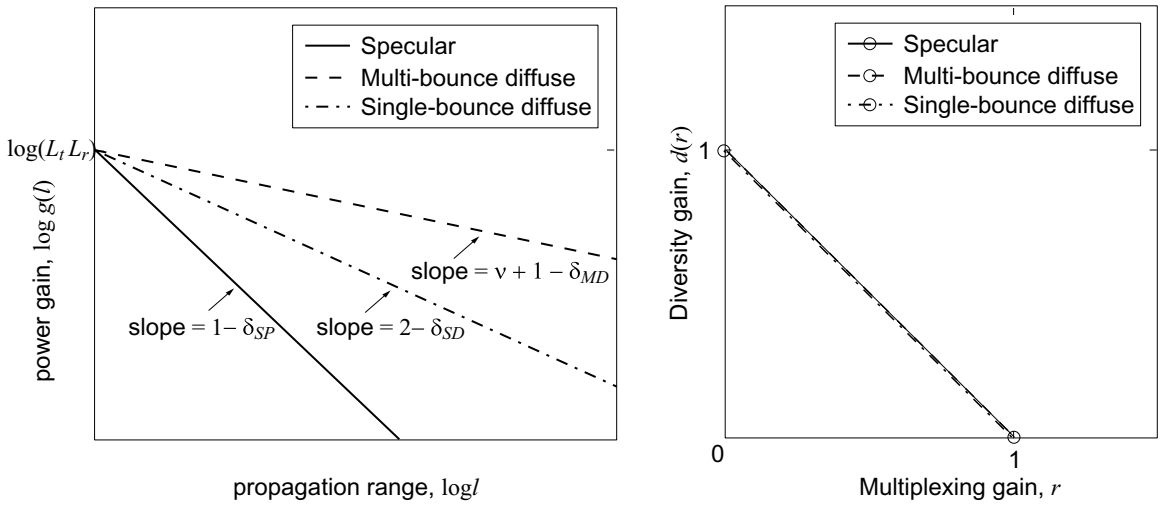

Figure 12: Illustrates the trade-off (left) between power gain and propagation range, and (right) between diversity gain and multiplexing gain in the specular, multi-bounce diffuse, and single-bounce diffuse channels.

channels. Later, we will show that they are different in other regimes. Finally, [25] proposes the trade-off formulation to compare different space-time codes and motivate a universal code design criterion for the particular i.i.d. fading channel. In this paper, we use the trade-off formulation to contrast different scattering mechanisms.

5 Large-Array Regime

The large-array regime refers to: $L_t|\Omega_t| \gg 1$ and $L_r|\Omega_r| \gg 1$. In this regime, the respective number of significant $\sigma_{t,m}$ and $\sigma_{r,n}$ are more than one. Therefore, we will first discuss the behavior of $\sigma_{t,m}$ with m and that of $\sigma_{r,n}$ with n in Section 5.1 as they will shape the dimension of the channel matrix. Then, we will derive the capacity of the specular channel in Secion 5.2 and that of the multi-bounce diffuse channel in Section 5.3. Based on which, we summarize the asymptotic capacity of various channels in Section 5.4 where we will draw several interesting points. After that, we will look into the trade-off between range and maximum multiplexing gain in Section 5.5, and the trade-off between multiplexing and diversity gains in Section 5.6. Finally, we will give a more comprehensive conclusion on the range-multiplexing-diversity trade-off in Section 5.7.

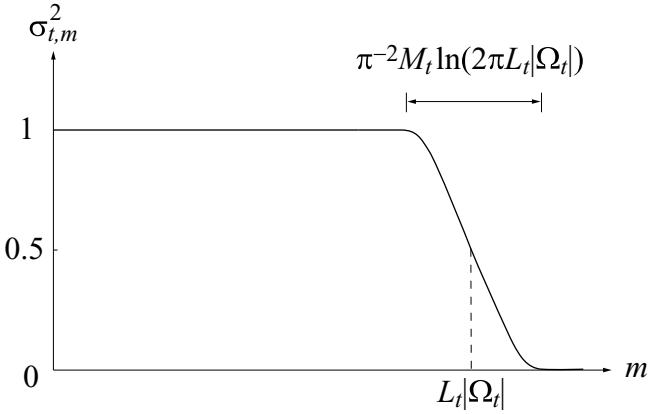

Figure 13: Plots the distribution of $\sigma^2_{t,m}$ for large $L_t|\Omega_t|$.

5.1 Properties of $\sigma_{t,m}$'s and $\sigma_{r,n}$'s

When $L_t|\Omega_t|$ is large, the number of $\sigma^2_{t,m}$ greater than x is given by

$$\bar{G}_t(x) = L_t|\Omega_t| + \frac{1}{\pi^2} M_t \ln(2\pi L_t|\Omega_t|) \ln \frac{1-x}{x} + o\big(\ln(L_t|\Omega_t|)\big) \tag{50}$$

as $L_t|\Omega_t| \to \infty$. This formula was first conjectured by Slepian in 1965 for the case when $M_t = 1$ [26]. It gave a precise interpretation of the $2WT$ degrees of freedom in a class of signals that are approximately time-limited to $[-T/2, T/2]$ and frequency-limited to $[-W, W]$ in [24]. Later in 1980, Landau and Widom proved the result for arbitrary M_t.

Fig. 13 plots the $\sigma^2_{t,m}$ versus m. For small $\epsilon > 0$, the number of $\sigma^2_{t,m}$ greater than $1-\epsilon$ is

$$\bar{G}_t(1-\epsilon) = L_t|\Omega_t| - \frac{\ln(1/\epsilon)}{\pi^2} M_t \ln(2\pi L_t|\Omega_t|) + o\big(\ln(L_t|\Omega_t|)\big)$$

while the number of $\sigma^2_{t,m}$ in between ϵ and $1-\epsilon$ is

$$\bar{G}_t(\epsilon) - \bar{G}_t(1-\epsilon) = \frac{2\ln(1/\epsilon)}{\pi^2} M_t \ln(2\pi L_t|\Omega_t|) + o\big(\ln(L_t|\Omega_t|)\big)$$

For a fixed ϵ, the ratio of the number of eigenvalues in the transition region (between 0 and 1) to those approaching 1 is approximately $M_t \ln(L_t|\Omega_t|)/(L_t|\Omega_t|)$ which is vanishingly small for large $L_t|\Omega_t|$. As the transition between the good and bad singular values is very abrupt (see Fig. 8 for $L_t = 64$), the number of spatial degrees of freedom can be easily identified [17]. However, when $L_t|\Omega_t|$ is not very large, the fraction of singular values in the transition region can no longer be ignored. In particular, the number of spatial degrees of freedom depends on the SNR, the number of scattering clusters M_t, and the disjointness of sub-intervals in Ω_t. We will discuss this later case in Section 6. Now, we derive the asymptotic cumulative distributions of $\sigma^2_{t,m}$ and $\sigma^2_{r,n}$ based on the Landau-Widom formula. These distributions will then be used to derive channel capacities.

Lemma 5.1. *Define*

$$G_t(x) := -\frac{1}{\pi^2} M_t \ln(2\pi L_t|\Omega_t|) \ln \frac{1-x}{x} \tag{51}$$

for $0 < x < \varepsilon_t$*, where* ε_t *satisfies*

$$\ln \frac{\varepsilon_t}{1-\varepsilon_t} = -\frac{\pi^2 L_t|\Omega_t|}{M_t \ln(2\pi L_t|\Omega_t|)} \tag{52}$$

For any increasing and bounded function $f(x)$*, we have*

$$\sum_{x\in\{\sigma^2_{t,m}\},\, x\geq a} f(x) = \int_a^{1-\varepsilon_t} f(x)\, dG_t(x) + o\big(\ln(L_t|\Omega_t|)\big) \tag{53}$$

Therefore, $G_t(x)$ *is the asymptotic cumulative distribution for* $\sigma^2_{t,m}$*.*

Similarly, the asymptotic cumulative distribution for $\sigma^2_{r,n}$ is

$$G_r(x) := -\frac{1}{\pi^2} M_r \ln(2\pi L_r|\Omega_r|) \ln \frac{1-x}{x} \tag{54}$$

for $0 < x < \varepsilon_r$, and ε_r satisfies

$$\ln \frac{\varepsilon_r}{1-\varepsilon_r} = -\frac{\pi^2 L_r|\Omega_r|}{M_r \ln(2\pi L_r|\Omega_r|)} \tag{55}$$

The proof is similar to that in [24, Lemma 8.5.3].

5.2 Capacity of Specular Channels

Following the same approach as in the small-array regime, we will first project the scattering response onto $\eta^*_{r,n}(\beta)\eta_{t,m}(\alpha)$ and obtain the (n,m)th element of the channel matrix:

$$\begin{aligned} H_{nm} &= \iint \eta^*_{r,n}(\beta) e^{-j\tau(\alpha)} \delta(\alpha-\beta) \eta_{t,m}(\alpha)\, d\alpha d\beta \\ &= \int e^{-j\tau(\alpha)} \eta^*_{r,n}(\alpha)\eta_{t,m}(\alpha)\, d\alpha \end{aligned}$$

To capture the essense of the deterministic nature of specular channels and account for the good angular resolvability of large arrays [17], we assume that

$$H_{nm} = e^{-j\tau_{nm}} \int \eta^*_{r,n}(\alpha)\eta_{t,m}(\alpha)\, d\alpha \tag{56}$$

When $L_t = L_r$,

$$H_{nm} = e^{-j\tau_{nn}} \delta_{nm} \tag{57}$$

yielding a diagonal channel matrix. When $L_t \neq L_r$, we expect the channel matrix mimics a band matrix with equal upper and lower bandwidth[4]. For simplicity, this paper focuses on $L_t = L_r$. The inputs and outputs are then related by

$$y_n = e^{-j\tau_{nn}}\sigma_{t,n}^2 x_n + z_n, \quad n \in \{1, 2, \cdots\} \tag{58}$$

The channel is composed of a multiple of parallel sub-channels. If the receiver estimates τ_{nn}, the channel capacity will be

$$C_{SP} = \sum_{x\in\{\sigma_{t,m}^2\}} \log(x^2\mu)^+ \tag{59}$$

where μ satisfies

$$\sum_{x\in\{\sigma_{t,m}^2\}} \Big(\mu - \frac{1}{x^2}\Big)^+ = \mathsf{SNR_t} \tag{60}$$

Applying Lemma 5.1 yields

$$C_{SP} = \int \big(\log(x^2\mu)\big)^+ dG_t(x) + o\big(\ln(L_t|\Omega_t|)\big) \tag{61}$$

and μ satisfies

$$\int \Big(\mu - \frac{1}{x^2}\Big)^+ dG_t(x) + o\big(\ln(L_t|\Omega_t|)\big) = \mathsf{SNR_t} \tag{62}$$

The computed result is summarized in the following lemma and the proof is included in Appendix A.

Lemma 5.2. *The capacity of the specular channel is*

$$C_{SP} = \Big[L_t|\Omega_t| + M_t \ln(2\pi L_t|\Omega_t|) f_1(\mathsf{SNR_t})\Big] \log\Big(1 + \frac{\mathsf{SNR_t}}{L_t|\Omega_t|}\Big) + o\big(\ln(L_t|\Omega_t|)\big) \tag{63}$$

as $L_t|\Omega_t| \to \infty$, *where*

$$f_1(\mathsf{SNR_t}) = \frac{1}{4\pi^2} \ln \frac{\mathsf{SNR_t}}{L_t|\Omega_t|} + o(\ln \mathsf{SNR_t}) \tag{64}$$

as $\mathsf{SNR_t} \to \infty$.

5.3 Capacity of Multi-bounce Diffuse Channels

Following the same reasoning as in (40), the (n, m)th element of the channel matrix is

$$H_{nm} = \iint \eta_{r,n}^*(\beta) h_{MD}(\beta, \alpha) \eta_{t,m}(\alpha)\, d\alpha d\beta \tag{65a}$$

$$\sim \frac{1}{l^{(\nu-1)/2}} \iint \eta_{r,n}^*(\beta) h_w(\beta, \alpha) \eta_{t,m}(\alpha)\, d\alpha d\beta \tag{65b}$$

$$\sim \frac{1}{l^{(\nu-1)/2}}\, \mathcal{CN}(0, 1) \tag{65c}$$

[4]A matrix $\mathbf{A}$ has a lower bandwidth p if $A_{nm} = 0$ whenever $n > m+p$ and upper bandwidth q if $m > n+q$ implies $A_{nm} = 0$.

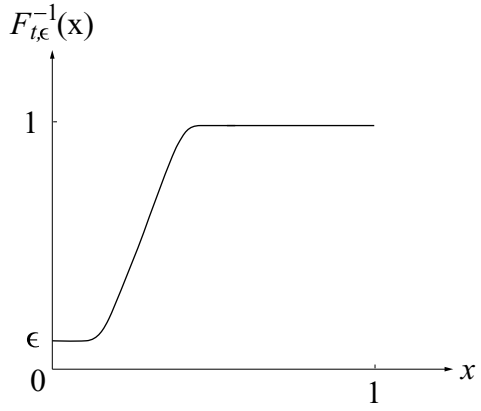

Figure 14: Plots the inverse map $F_{t,\epsilon}^{-1}(x)$.

In addition, the circularly symmetric property of $h_w(\beta, \alpha)$ asserts that H_{nm}'s are independent. Consequently, the channel matrix is an i.i.d. complex Gaussian random matrix. Now, the statistical properties of the channel matrix do not depend on the detail of the basis functions which is a very convenient property. Also, note that the asymptotic cumulative distribution of $\sigma_{t,m}$ depends on the product $L_t|\Omega_t|$ and M_t only (Lemma 5.1). That is, two channels with different Ω_t but same measure $|\Omega_t|$ and same number of disjoint sub-intervals M_t will yield the same performance for large L_t. For simplicity, this paper therefore focuses on the scenario where $L_t|\Omega_t| = L_r|\Omega_r|$ and $M_t = M_r$. That is, the asymptotic cumulative distributions of $\sigma_{t,m}$ and $\sigma_{r,n}$ are approximately the same.

If the channel matrix is known at the receiver but unknown at the transmitter, the ergodic channel capacity will be

$$C_{MD} = \max_{\mathbf{K} \succ 0,\, \mathrm{tr}(\mathbf{K}) \leq \mathsf{SNR_t}} \mathsf{E}_{\mathbf{H}} \left[\log \det(\mathbf{I} + \mathbf{\Sigma}_t \mathbf{H} \mathbf{\Sigma}_t \mathbf{K} \mathbf{\Sigma}_t \mathbf{H}^\dagger \mathbf{\Sigma}_t) \right] \tag{66}$$

where $\mathbf{\Sigma}_t$ is a diagonal matrix with the nth diagonal element equal to $\sigma_{t,n}$. Accordingly, the optimal covariance matrix $\mathbf{K}$ is diagonal as $\mathbf{\Sigma}_t$ is diagonal. The dimension of $\mathbf{H}$, however, is unknown *a priori*. Tools from random matrix theory can be applied to obtain a lower bound only. An upper bound is also derived. Then we will show that they are asymptotically tight.

Lower Bound

If we consider only those $\sigma_{t,m}^2$'s greater than ϵ and pour equal power over them, this will give a lower bound for C_{MD}. Recall that $\bar{G}_t(\epsilon)$ gives the number of $\sigma_{t,m}^2$ greater than ϵ. We define the empirical distribution of $\sigma_{t,m}^2$ by

$$F_{t,\epsilon}(x) := \frac{\bar{G}_t(\epsilon) - \bar{G}_t(x)}{\bar{G}_t(\epsilon)} \tag{67}$$

Fig. 14 plots the inverse map $F_{t,\epsilon}^{-1}(x)$, compared to Fig. 13. For a fixed ϵ, as $L_t|\Omega_t|$ increases, random matrix results in Girko [27] can be applied to obtain the limiting eigenvalue distribution of $l^{1-\nu}\mathbf{\Sigma}_{t,\epsilon}^2\mathbf{H}_\epsilon\mathbf{\Sigma}_{t,\epsilon}^2\mathbf{H}_\epsilon^\dagger$, denoted by $F_c(x)$. Submatrices $\mathbf{\Sigma}_{t,\epsilon}$ and $\mathbf{H}_\epsilon$ contain the first $\bar{G}_t(\epsilon)$ rows and columns of $\mathbf{\Sigma}_t$ and $\mathbf{H}$ respectively. [5] showed that the Steltjes' transform[5] of $F_c(x)$ is given by

$$m_{F_c}(z) = \int_0^1 u(x,z)\,dx$$

and $u(x,z)$ is the unique solution to the fixed-point equation

$$u(x,z) = \Big[-z + F_{t,\epsilon}^{-1}(x)\int_0^1 \frac{F_{t,\epsilon}^{-1}(p)\,dp}{1 + F_{t,\epsilon}^{-1}(p)\int_0^1 u(q,z)F_{t,\epsilon}^{-1}(q)\,dq}\Big]^{-1}$$

Hence, C_{MD} is lower-bounded by

$$C_{MD} \geq \bar{G}_t(\epsilon)\int_0^\infty \log\Big(1 + \frac{\mathsf{SNR_t}}{l^{\nu-1}}x\Big)\,dF_c(x) \tag{68}$$

as $L_t|\Omega_t| \to \infty$. At high SNR, [5] obtains the following approximation:

$$C_{MD} \gtrsim \bar{G}_t(\epsilon)\Big[\log\frac{\mathsf{SNR_t}}{l^{\nu-1}e} + 2\int_0^1 \log F_{t,\epsilon}^{-1}(x)\,dx\Big] \tag{69a}$$

$$= \bar{G}_t(\epsilon)\Big[\log\frac{\mathsf{SNR_t}}{l^{\nu-1}e} + 2\int_\epsilon^1 \log x\,dF_{t,\epsilon}(x)\Big] \tag{69b}$$

The lower-bound is computed and summarized in the following lemma, and the proof is included in Appendix B.

Lemma 5.3. *The ergodic capacity of the multi-bounce diffuse channel is approximately lower-bounded by*

$$C_{MD} \gtrsim \Big[L_t|\Omega_t| + M_t\ln(2\pi L_t|\Omega_t|)f_2(\mathsf{SNR_t})\Big]\log\frac{\mathsf{SNR_t}}{l^{\nu-1}e} + o\big(\ln(L_t|\Omega_t|)\big) \tag{70}$$

as $L_t|\Omega_t| \to \infty$, *where*

$$f_2(\mathsf{SNR_t}) = \frac{1}{4\pi^2}\ln\frac{\mathsf{SNR_t}}{l^{\nu-1}} + o(\ln\mathsf{SNR_t}) \tag{71}$$

as $\mathsf{SNR_t} \to \infty$.

Upper Bound

[5]The Steltjes' transform of a distribution $F(\cdot)$ is defined by

$$m_F(z) := \int \frac{1}{x-z}\,dF(x)$$

As all $\sigma_{t,m}^2$'s are less than 1, we have

$$tr(\mathbf{\Sigma}_t \mathbf{K} \mathbf{\Sigma}_r) < tr(\mathbf{K})$$

Hence, C_{MD} is upper-bounded by

$$C_{MD} \leq \max_{\mathbf{K} \succ 0,\, \mathrm{tr}(\mathbf{K}) \leq \mathsf{SNR_t}} \mathsf{E}_{\mathbf{H}} \left[\log_2 \det(\mathbf{I} + \mathbf{\Sigma}_t \mathbf{H} \mathbf{K} \mathbf{H}^\dagger \mathbf{\Sigma}_t) \right] \tag{72}$$

Furthermore, $\log \det$ is concave so the bound is relaxed to

$$C_{MD} \leq \sum_m \log_2(1 + \mathsf{SNR_t} \sigma_{t,m}^2) \tag{73}$$

The upper-bound is computed and summarized in the following lemma, and the proof is included in Appendix C.

Lemma 5.4. *The ergodic capacity of the multi-bounce diffuse channel is upper-bounded by*

$$C_{MD} \leq \Big[L_t|\Omega_t| + M_t \ln(2\pi L_t|\Omega_t|) f_3(\mathsf{SNR_t}) \Big] \log\Big(1 + \frac{\mathsf{SNR_t}}{l^{\nu-1}}\Big) + o\big(\ln(L_t|\Omega_t|)\big) \tag{74}$$

as $L_t|\Omega_t| \to \infty$, *where*

$$f_3(\mathsf{SNR_t}) = \frac{1}{2\pi^2} \ln \frac{\mathsf{SNR_t}}{l^{\nu-1}} + o(\ln \mathsf{SNR_t}) \tag{75}$$

as $\mathsf{SNR_t} \to \infty$.

5.4 Maximum Spatial Multiplexing Gain

Theorem 5.5. *Suppose* Ω_t *and* Ω_r *are known a priori at the transmitter and the receiver respectively.*

- Specular channels. *Assume* $L_t = L_r$. *The channel capacity* C_{SP} *is*

$$C_{SP} = L_t|\Omega_t| \log\Big(1 + \frac{\mathsf{SNR_t}}{L_t|\Omega_t|}\Big) + o(L_t|\Omega_t|) \tag{76}$$

  as $L_t|\Omega_t| \to \infty$.

- Multi-bounce diffuse channels. *Assume* $L_t|\Omega_t| = L_r|\Omega_r|$, $M_t = M_r$, *and elements of the channel matrix* H_{nm}*'s are known at the receiver but unknown at the transmitter. The ergodic capacity* C_{MD} *is bounded by*

$$L_t|\Omega_t| \log \frac{\mathsf{SNR_t}}{l^{\nu-1} e} + o(L_t|\Omega_t|) \lesssim C_{MD} \leq L_t|\Omega_t| \log\Big(1 + \frac{\mathsf{SNR_t}}{l^{\nu-1}}\Big) + o(L_t|\Omega_t|) \tag{77}$$

  as $L_t|\Omega_t| \to \infty$.

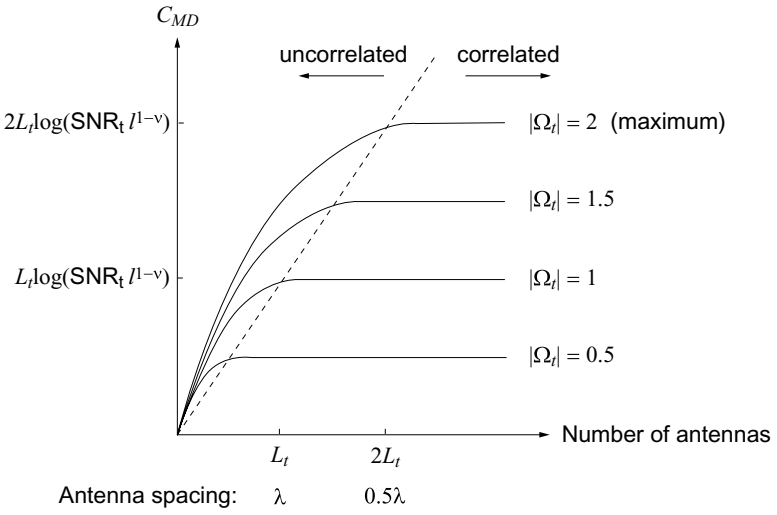

Figure 15: Illustrates the impact of scattering on capacity for fixed length of antenna arrays ($L_t = L_r$) and $\mathsf{SNR_t}$.

- Single-bounce diffuse channels. *Assume* $L_t|\Omega_{t,i}| = L_r|\Omega_{r,j}| = \frac{L_t|\Omega_t|}{M_t}$ *for all* i, j, M_t *is finite, and elements of the channel matrix* H_{nm}*'s are known at the receiver but unknown at the transmitter. The ergodic capacity* C_{SD} *is bounded by*

$$L_t|\Omega_t| \log \frac{\mathsf{SNR_t}}{M_t e} + o(L_t|\Omega_t|) \lesssim C_{SD} \leq L_t|\Omega_t| \log\Big(1 + \frac{\mathsf{SNR_t}}{M_t}\Big) + o(L_t|\Omega_t|) \qquad (78)$$

  as $L_t|\Omega_t| \to \infty$.

Theorem 5.5 summaries the asymptotic capacity results. When L_t and L_r are large, the single-bounce diffuse channel is approximately equivalent to M_t independent single-cluster multi-bounce diffuse channels. Fischer's inequality assures that the optimal input covariance is separable among the M_t parallel clustered channels. Asymptotic results from multi-bounce diffuse channel are then applied to obtain the asymptotic capacity of single-bounce diffuse channels. All channels have the same asymptotic number of spatial degrees of freedom equal to $L_t|\Omega_t|$ – the maximum spatial multiplexing gain. It is insensitive to the underlying scattering mechanisms. This aligns with the degree-of-freedom result in [17] where scattering mechanisms are not modeled.

The capacity results lead us to have a different perspective on:

- *Antenna correlation.* Fixing L_t and L_r, Fig. 15 plots the channel capacity (C_{MD}) versus the number of antennas and channel angular bandwidth. At a particular channel angular bandwidth, channel capacities saturate as the number of antennas increases and therefore, they are not increasing linearly with the number of antennas. Instead,

Table 2: Power gain per spatial channel.

Scattering mechanisms	Small-array regime	Large-array regime
Specular	$L_t L_r \lvert\Omega_t\rvert$	1
Multi-bounce diffuse	$\frac{L_t L_r \lvert\Omega_t\rvert\lvert\Omega_r\rvert}{l^{\nu-1}}$	$\frac{L_t \lvert\Omega_t\rvert}{l^{\nu-1}}$
Single-bounce diffuse	$\frac{L_t L_r \lvert\Omega_t\rvert\lvert\Omega_r\rvert}{M_t}$	$\frac{L_t \lvert\Omega_t\rvert}{M_t}$

the channel can be made less correlated by using fewer antennas and not fully utilizing the available channel angular bandwidth, or it can be made highly correlated and fully utilized the channel angular bandwidth at the expense of more antennas. The dotted line in the figure shows the transition. Conventionally, the quality of a multiple-antenna channel is justified by the correlation across different pairs of antennas. This antenna correlation, however, is a consequence of the trade-off between performance and the number of antennas used (or cost). Therefore, it is not fair to justify the quality of a channel based on the antenna correlation.

- *Minimum antenna spacing.* The maximum multiplexing gain cannot be increased indefinitely by exploring the scattering nature of physical environments. Because the channel angular bandwidth is upper-bounded by the extent of the propagation space. For linear arrays, $|\Omega_t|$ and $|\Omega_r|$ are less than or equal to 2. Therefore, in a fully scattered environment, the maximum multiplexing gain is $2L_t$, and $2L_t$ number of antennas corresponds to the well-established half-wavelength antenna spacing criterion from antenna theory. The criterion given in [1] based on the antenna correlation derived from a statistical single-cluster model is somewhat optimistic. It showed that the minimum antenna spacing is 0.382 wavelength for linear arrays. The inconsistency stems from the use of $d\theta$ instead of $d\cos\theta$ as the differetial in (25). Otherwise, both criteria should coincide. However, the former involves no assumption on the channel statistics.

- *Capacity scaling.* For a given $|\Omega_t|$ and fixed antenna spacing, the channel capacity increases with the number of antennas due to an increase in the total length of antenna arrays. This linear growth holds in a richly scattered environment (larger $|\Omega_t|$) as well as in a less scattered environment (smaller $|\Omega_t|$). Thus, it is also not fair to assert that the capacity scaling in multiple-antenna systems occurs in richly scattered environments.

The underlying scattering mechanisms affect the power gain per spatial channel, like that in the small-array regime. Table 2 summaries these gains. Larger arrays have a better

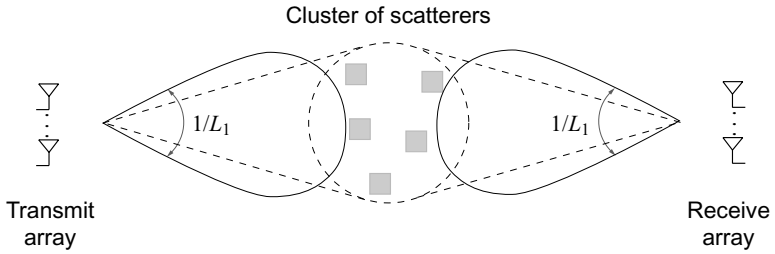

(a) Small-array regime

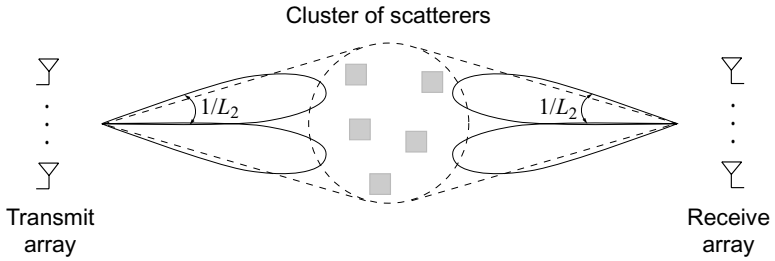

(b) Large-array regime, $L_2 >> L_1$

Figure 16: Contrasts the power transfer and the creation of spatial channels in the small-array and large-array regimes. Note that the beams plotted are over-simplified to ease explanation and do not reflect the actual $\Xi_{t,m}(\cdot)$ and $\Xi_{r,n}(\cdot)$.

angular resolution and are able to generate narrower beams. A narrower beam improves the energy transfer as illustrated in Fig. 16(a). When the array length is substantial, more beams can be fitted within the sub-intervals of Ω_t as shown in Fig. 16(b). The transmit power is now split up to support multiple spatial channels with $\mathsf{SNR_t}/(L_t|\Omega_t|)$ each. However, unlike the small-array regime, the fraction of this transmit power being relayed by scatterers is *unity* because the entire beam is within Ω_t. The receive power then depends on the underlying scattering mechanisms:

- In specular channels, as the transmit and receive directions are in one-to-one correspondence, the receive power per spatial channel is

$$\mathsf{SNR_r} = \frac{\mathsf{SNR_t}}{L_t|\Omega_t|}$$

  that is, the power gain per spatial channel is unity.

- In multi-bounce diffuse channels, as the transmit power is spread over the entire Ω_r, the receive power per spatial channel is therefore scaled up by $L_r|\Omega_r|$ $(= L_t|\Omega_t|)$,

$$\mathsf{SNR_r} = \frac{\mathsf{SNR_t}}{l^{\nu-1}} = \frac{L_t|\Omega_t|}{l^{\nu-1}} \cdot \frac{\mathsf{SNR_t}}{L_t|\Omega_t|}$$

This phenomenon is similar to the spreading gain in waveform channels where a data symbol can be spread over multiple time-samples and/or sub-carriers to increase the robustness against channel fading. In waveform channels, the spreading is done *explicitly* whereas in multiple-antenna channels, the secondary-source property of diffuse scattering/diffraction brings forth the spreading *implicitly*.

- In single-bounce diffuse channels, the transmit power emanated from $\Omega_{t,i}$ is spread over $\Omega_{r,i}$ so the receive power per spatial channel is scaled up by $L_r|\Omega_{r,i}|$ $(= L_t|\Omega_t|/M_t)$ instead,

$$\mathsf{SNR_r} = \frac{\mathsf{SNR_t}}{M_t} = \frac{L_t|\Omega_t|}{M_t} \cdot \frac{\mathsf{SNR_t}}{L_t|\Omega_t|}$$

Plausibly, multi-bounce diffuse channels are more favorable. However, they have the worst path loss, being scaled down by $l^{\nu-1}$. The amount of spreading and path loss counteract each other. As a result, the multi-bounce diffuse channel is better for short range and high data rate transmission, while the specular channel is better for longer range but lower data rate transmission. The single-bounce diffuse channel enjoys both sides of the coin. Similar observation is reported in [28].

In [7, 10], channel capacities are shown to be increasing with less connectivity between the transmit and receive propagation spaces. Ignoring path loss, they imply that single-bounce diffuse channels have better ergodic performance than multi-bounce diffuse channels. The inconsistency stems from [7, 10] keeping the receive SNR per spatial channel constant. That is, the transmit SNR in the single-bounce diffuse channel will be M_t times more than that in the multi-bounce diffuse channel. Not surprisingly, the ergodic performance is in favor of the single-bounce diffuse channel.

Finally, at high SNR the capacity formulas derived in Lemma 5.2–5.4 can be approximated by

$$C_{SP} \approx \left[L_t|\Omega_t| + \frac{1}{4\pi^2} M_t \ln(2\pi L_t|\Omega_t|) \ln \frac{\mathsf{SNR_t}}{L_t|\Omega_t|}\right] \log \frac{\mathsf{SNR_t}}{L_t|\Omega_t|} \tag{79a}$$

$$C_{MD} \approx \left[L_t|\Omega_t| + \frac{1}{c\pi^2} M_t \ln(2\pi L_t|\Omega_t|) \ln \frac{\mathsf{SNR_t}}{l^{\nu-1}}\right] \log \frac{\mathsf{SNR_t}}{l^{\nu-1}} \tag{79b}$$

for some constant $c \in (2, 4)$. Apparently, there is an addition of $\frac{1}{4\pi^2} M_t \ln(2\pi L_t|\Omega_t|) \ln \frac{\mathsf{SNR_t}}{L_t|\Omega_t|}$ degrees of freedom in the specular channel and $\frac{1}{c\pi^2} M_t \ln(2\pi L_t|\Omega_t|) \ln \frac{\mathsf{SNR_t}}{l^{\nu-1}}$ in the multi-bounce diffuse channel. These additional degrees of freedom as compared to $L_t|\Omega_t|$ is negligble as $L_t|\Omega_t| \to \infty$ but become increasingly significant as $L_t|\Omega_t|$ is finite. Here we point out this interesting observation which will be elaborated more at the finite-array regime in Section 6.

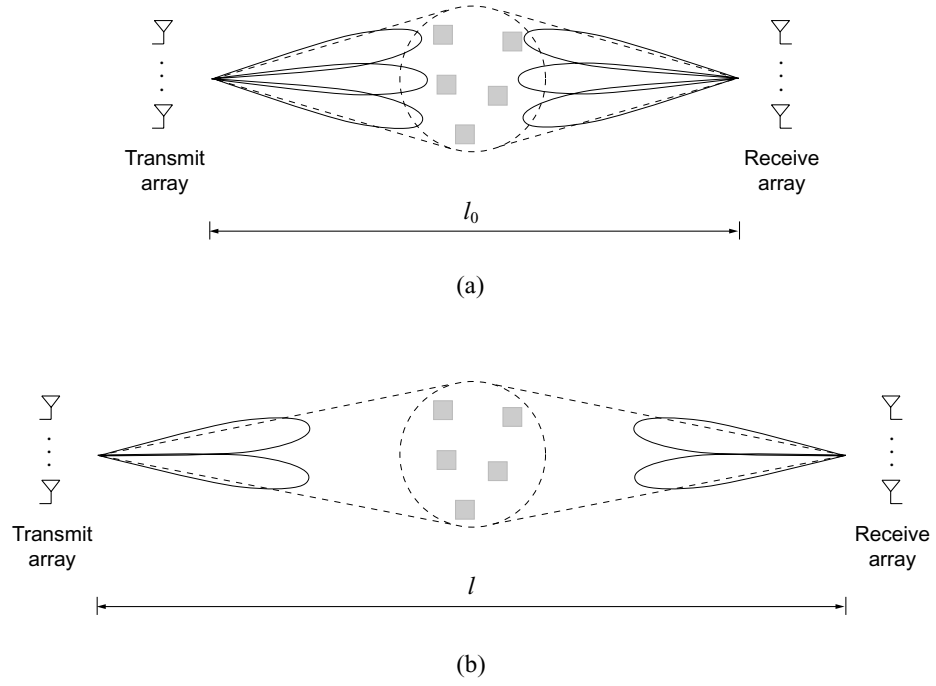

Figure 17: A range-multiplexing trade-off example where (a) shows the angular bandwidth at the reference range of l_0 and (b) illustrates the decrease in the number of spatial channels at propagation range of l. Note that the beams plotted are over-simplified to ease explanation and do not reflect the actual $\Xi_{t,m}(\cdot)$ and $\Xi_{r,n}(\cdot)$.

5.5 Range-Multiplexing Trade-offs

Usually, range extension relates to beamforming to the strongest spatial channel, and therefore there should not be any trade-off between propagation range and spatial degrees of freedom. However, it can be carried out more sophisticatedly by beamforming to the first few strongest spatial channels. For example, one originally transmits with N_1 spatial degrees of freedom and now wants to extend the propagation range by focusing all energy on the first N_2 ($< N_1$) strongest degrees of freedom. Now, increasing the propagation range presumably decreases the channel angular bandwidth as suggested by Hypothesis 4.1. This will put forth an upper bound on N_2. This section therefore devotes to quantify the trade-off between propagation range and this bound.

Applying Hypothesis 4.1, the maximum spatial multiplexing gain at a propagation range of l is

$$r_0(l) = \frac{1}{l} L_t |\Omega_{t0}| \tag{80}$$

which gives the range-multiplexing trade-off curve. Fig. 17 gives an example of this trade-off. In the small array regime, the trade-off between range and power gain is very sensitive

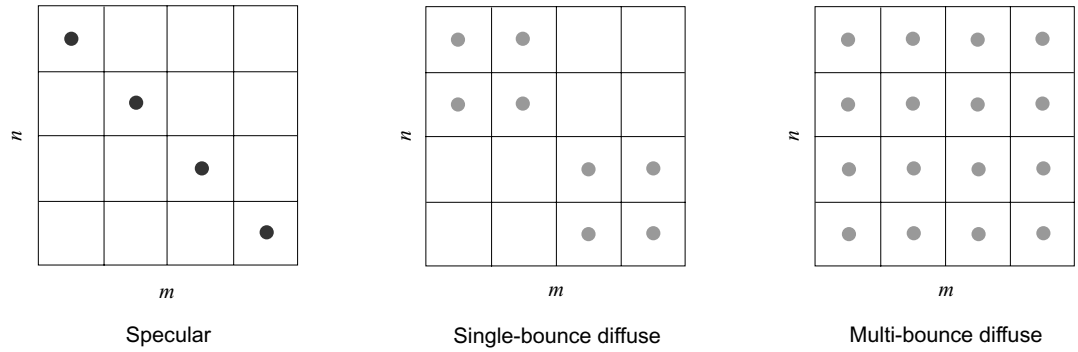

Figure 18: Illustrates differences in the channel matrix among specular, single-bounce diffuse, and multi-bounce diffuse channels. Each small dot represents the matrix element being non-zero. A darker dot means the element being deterministic while a ligher dot means the element being a zero-mean complex Gaussian random variable independent of others.

to the underlying scattering mechanisms (see Fig. 12). Here, the trade-off between range and maximum multiplexing gain is insensitive to these mechanisms.

The formula is very simple. Imagine if one attempts to study this trade-off using the standard MIMO model for multiple-antenna systems, one would need to model the effect of propagation range on the antenna correlation and then indirectly infer the trade-off from an increase in the antenna correlation with increasing propagation range. Here, we demonstrate a more direct approach.

5.6 Multiplexing-Diversity Trade-offs

Unlike the small-array regime, now the channel matrix varies with the underlying scattering mechanisms as contrasted in Fig. 18. As there are asymptotically $L_t|\Omega_t|$ significant $\sigma^2_{t,m}$ and $L_r|\Omega_r|$ significant $\sigma^2_{r,n}$, and these eigenvalues are all asymptotically equal to 1, the multi-bounce diffuse channel is approximately mimic the standard i.i.d. fading model for multiple-antenna systems. The maximum diversity gain is therefore $L_tL_r|\Omega_t||\Omega_r|$. Similarly, the single-bounce diffuse channel is approximately

$$\mathbf{y} = \begin{bmatrix} \mathbf{H}_1 & & \mathbf{0} \\ & \ddots & \\ \mathbf{0} & & \mathbf{H}_{M_t} \end{bmatrix} \mathbf{x} + \mathbf{z} \tag{81}$$

where $\mathbf{H}_i \sim \mathcal{CN}\big(\mathbf{0}, \mathbf{I}_{L_r|\Omega_{r,i}|} \otimes \mathbf{I}_{L_t|\Omega_{t,i}|}\big)$ for $i = 1, \cdots, M_t$. The maximum diversity gain becomes $\sum_i L_tL_r|\Omega_{t,i}||\Omega_{r,i}|$. Table 3 summaries these diversity orders.

Underlying scattering mechanisms not only affect the maximum diversity gain but also the trade-offs between diversity and multiplexing gains. Following the formulation proposed

Table 3: Maximum diversity gain.

Scattering mechanisms	Small-array regime	Large-array regime
Specular	1	∞
Multi-bounce diffuse	1	$L_t L_r \lvert\Omega_t\rvert\lvert\Omega_r\rvert < \infty$
Single-bounce diffuse	1	$\sum_i L_t L_r \lvert\Omega_{t,i}\rvert\lvert\Omega_{r,i}\rvert \leq L_t L_r \lvert\Omega_t\rvert\lvert\Omega_r\rvert$

in [25] (see Definition 4.2), the trade-off curve for the multi-bounce diffuse channel is given by solving

$$\lim_{\mathsf{SNR_r}\to\infty} \frac{\log P\big[\det(\mathbf{I} + \frac{\mathsf{SNR_r}}{L_t|\Omega_t|}\mathbf{H}_w^\dagger \mathbf{H}_w) < \mathsf{SNR_r}^r\big]}{\log \mathsf{SNR_r}} = -d_{MD}(r) \tag{82}$$

where $\mathbf{H}_w \sim \mathcal{CN}\big(\mathbf{0}, \mathbf{I}_{L_t|\Omega_t|} \otimes \mathbf{I}_{L_t|\Omega_t|}\big)$. Similarly, the trade-off curve for the single-bounce diffuse channel is given by solving

$$\lim_{\mathsf{SNR_r}\to\infty} \frac{\log P\big[\prod_{i=1}^{M_t} \det(\mathbf{I} + \frac{\mathsf{SNR_r}}{L_t|\Omega_{t,i}|}\mathbf{H}_i^\dagger \mathbf{H}_i) < \mathsf{SNR_r}^r\big]}{\log \mathsf{SNR_r}} = -d_{SD}(r) \tag{83}$$

The trade-off curve for the multi-bounce diffuse channel is the same as the i.i.d. fading channel solved in [25]. Here, we solve the trade-off curve for the single-bounce diffuse channel. The results are summarized in Theorem 5.6.

Theorem 5.6. *Suppose Ω_t and Ω_r are known a priori at the transmitter and the receiver respectively, and the channel matrix is known at the receiver but unknown at the transmitter. Define*

$$r_0 := \min\big\{L_t|\Omega_t|, L_r|\Omega_r|\big\}$$

- Multi-bounce diffuse channels. *The trade-off curve $d_{MD}(r)$ is given by a piecewise linear function connecting the points $(r, d_{MD}(r))$, $r = 0, \cdots, r_0$, where*

$$d_{MD}(r) = (L_t|\Omega_t| - r)(L_r|\Omega_r| - r) \tag{84}$$

- Single-bounce diffuse channels. *The trade-off curve $d_{SD}(r)$ is*

$$d_{SD}(r) = d_1(r) \oplus d_2(r) \oplus \cdots \oplus d_{M_t}(r) \tag{85}$$

where $d_i(r)$ is a piecewise linear function connecting the points $(r, d_i(r))$, $r = 0, \cdots, \min\{L_t|\Omega_{t,i}|, L_t|\Omega_{r,i}|\}$ and

$$d_i(r) = (L_t|\Omega_{t,i}| - r)(L_r|\Omega_{r,i}| - r) \tag{86}$$

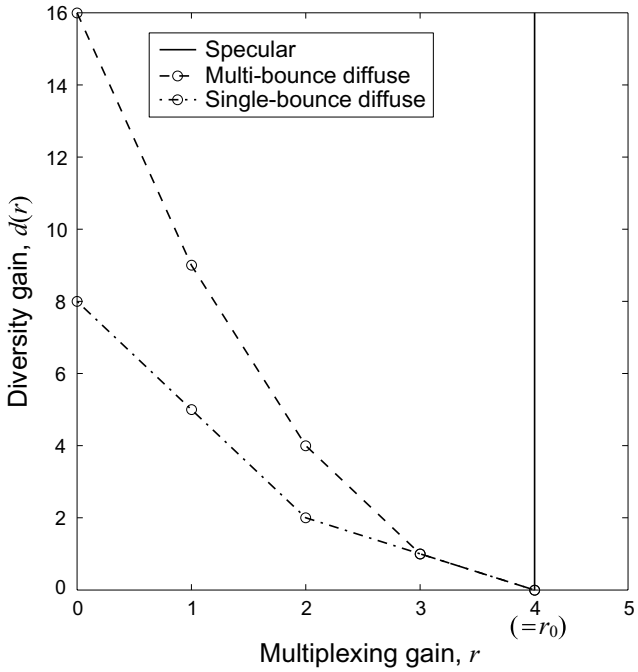

Figure 19: Contrasts the multiplexing-diversity trade-off curves for the specular, multi-bounce diffuse, and single-bounce diffuse channels where $M_t = M_r = 2$, $L_t|\Omega_{t,i}| = 2$, and $L_r|\Omega_{r,i}| = 2$ for $i = 1, 2$.

The operation $\oplus$ denotes the min-plus convolution and is defined as

$$(f \oplus g)(t) = \inf_{0 \le s \le t} \big\{ f(t-s) + g(s) \big\} \tag{87}$$

Descriptively, the trade-off curve is obtained by putting end-to-end the different linear pieces in $d_i(r)$'s, sorted by increasing slopes (or equivalently, decreasing negative slopes).

The proof for $d_{SD}(\cdot)$ is included in Appendix D. For example, if the number of disjoint sub-intervals in Ω_t and Ω_r are equal and the respective sub-intervals are of equal length, then $d_{SD}(r)$ is the piecewise linear function connecting the points $(m, d_{SD}(r))$, $r = 0, M_t, \cdots, r_0$, where

$$d_{SD}(r) = \frac{1}{M_t}(L_t|\Omega_t| - r)(L_r|\Omega_r| - r) \tag{88}$$

Comparing with $d_{MD}(r)$ in (84), the multi-bounce diffuse channel achieves an M_t-fold better diversity gain than the single-bounce diffuse channel in supporting a multiplexing gain which is a multiple of M_t, as illustrated in Fig. 19.

Compared to Fig. 12, the impact of scattering mechanisms on performances is more distinguishable. Two points are noteworthy

- *Randomness of channel matrices.* Large antenna arrays have fine angular resolution, and therefore are able to separate reflected paths finely and remove the randomness from the aggregation of many paths[6]. However, the randomness in diffuse channels is due to the aggregation of many paths within the scattering source. Even the antenna array has very good angular resolution, it still cannot remove the inherent randomness.

- *Space-time code design.* The trade-off curves are no longer identical unlike those in the small-array regime. Recent space-time code design mainly focuses on the i.i.d. fading channel (equivalent to the multi-bounce diffuse channel). However, real channels are more specular and single-bounce diffuse in nature[7]. Understanding these differences on trade-offs, sheds light on designing more efficient space-time coding schemes that can adapt to the physical environment. Imagine if we design a space-time code that is optimal for the i.i.d fading channel and use it in a single-bounce diffuse channel, the link reliability can be much worse, particularly for large systems.

Finally, it is possible to turn a single-bounce diffuse channel into a multi-bounce diffuse channel by increasing the antenna spacing. This plausibly increases the diversity gain and validate the performance analyses based on the i.i.d. fading model. However, when the array length is fixed, using less antennas decreases the spatial degrees of freedom. The resulting trade-off curve is upper-bounded by the curve given in Theorem 5.6. That is, the transceiver is not utilizing all the available channel resources given by nature in order to justify the i.i.d. fading model.

5.7 Range-Multiplexing-Diversity Trade-offs

A multiple-antenna system can improve the propagation range, data rate, and probability of error. All these benefits can be achieved simultaneously but there is a trade-off among them. The following corollary summaries this trade-off in terms of the channel angular bandwidth and the underlying scattering mechanisms. To achieve a propagation range of l, the maximum multiplexing gain available is $r_0(l)$ which depends on the channel angular bandwidth, $|\Omega_t|$ and $|\Omega_r|$. Now, one can sacrifice some of this multiplexing gain to obtain certain diversity gain where this trading depends on the underlying scattering mechanisms. Fig. 20 gives an example of this trade-off where it succinctly illustrates the impact of scattering on the achievable performance of a multiple-antenna system.

Corollary 5.7. *Suppose Ω_t and Ω_r are known a priori at the transmitter and the receiver respectively, and the channel matrix is known at the receiver but unknown at the transmitter.*

[6]As another example, the familiar r^{-4} path loss for a channel with a direct path and a ground reflected path [19] can be resolved back to the path loss of r^{-2} if the antenna array is large enough to separate the two paths.

[7]From channel measurements, typical path-loss exponent is between 2 and 4.

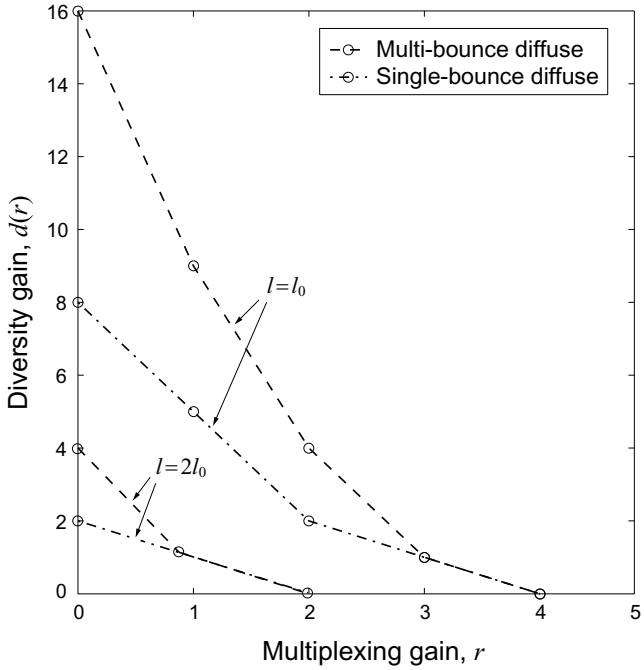

Figure 20: Illustrates the multiplexing-diversity-range trade-offs when $M_t = M_r = 2$ and $N_{t,i} = N_{r,j} = 2$ at $l = l_0$ and $2l_0$.

- Multi-bounce diffuse channels. *The trade-off curve $d_{MD}(l, r)$ is given by a piecewise linear function connecting the points*

$$d_{MD}(l,r) = \Big(\frac{L_t|\Omega_{t0}|}{l} - r\Big)\Big(\frac{L_r|\Omega_{r0}|}{l} - r\Big), \quad r = 0, \cdots, \min\Big\{\frac{L_t|\Omega_{t0}|}{l}, \frac{L_r|\Omega_{r0}|}{l}\Big\} \quad (89)$$

- Single-bounce diffuse channels. *The trade-off curve $d_{SD}(r)$ is*

$$d_{SD}(l,r) = d_1(l,r) \oplus d_2(l,r) \oplus \cdots \oplus d_{M_t}(l,r) \quad (90)$$

where $d_i(l, r)$ is a piecewise linear function connecting the points

$$d_i(l,r) = \Big(\frac{L_t|\Omega_{t0,i}|}{l} - r\Big)\Big(\frac{L_r|\Omega_{r0,i}|}{l} - r\Big), \quad r = 0, \cdots, \min\Big\{\frac{L_t|\Omega_{t0,i}|}{l}, \frac{L_r|\Omega_{r0,i}|}{l}\Big\} \quad (91)$$

where $|\Omega_{t0,i}|$ and $|\Omega_{r0,i}|$ are the respective transmit and receive angular bandwidth subtended by the ith scattering cluster at the reference range l_0.

6 Finite-Array Regime

The finite-array regime is in between the small-array and large-array regimes. Insights developed in those two regimes now guide the intuition for the finite-array regime where

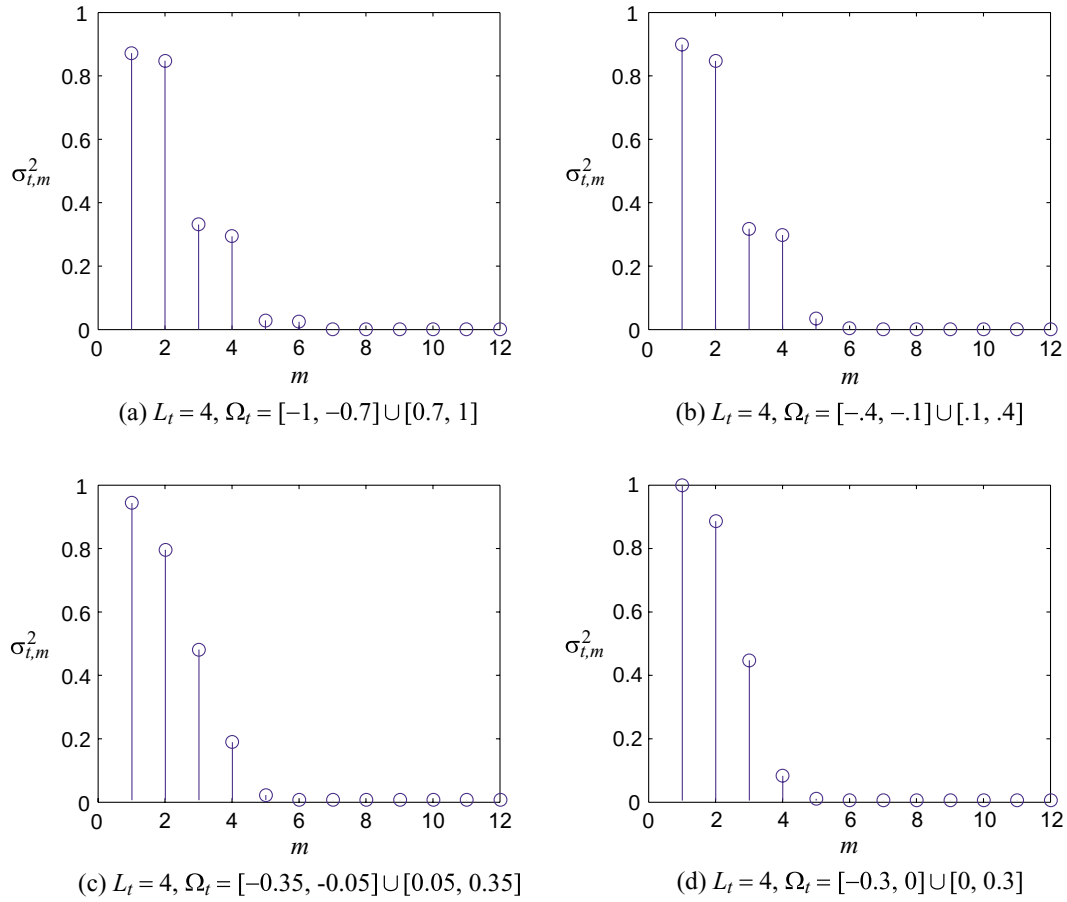

Figure 21: Plots the distribution of $\sigma_{t,m}$ for $L_t = 4$ and different $|\Omega_t| = 0.6$.

heuristic reasonings will be developed. We will focus the discussion on the maximum spatial multiplexing gain and diversity gain.

6.1 Spatial Multiplexing Gain

The integral kernels in (30) have infinite number of non-zero singular values, $\sigma_{t,n}$ and $\sigma_{r,n}$. At the large-array regime, the transition between good and bad singular values is so abrupt that the significant singular values are mostly the same and approximately equal to 1. The distribution of $\sigma_{t,m}$ and that of $\sigma_{r,n}$ depend on the respective measure $|\Omega_t|$ and $|\Omega_r|$. At the finite-array regime, however, the transition is leveled off (see Fig. 8) and those distributions now depend on the angular positions of scattering clusters, that is, the set Ω_t and Ω_r. To gain some intuitions, consider a multiple-antenna system with $L_t = 4$ ($1/L_t = 0.25$) in physical environments having 2 scattering clusters of equal angular

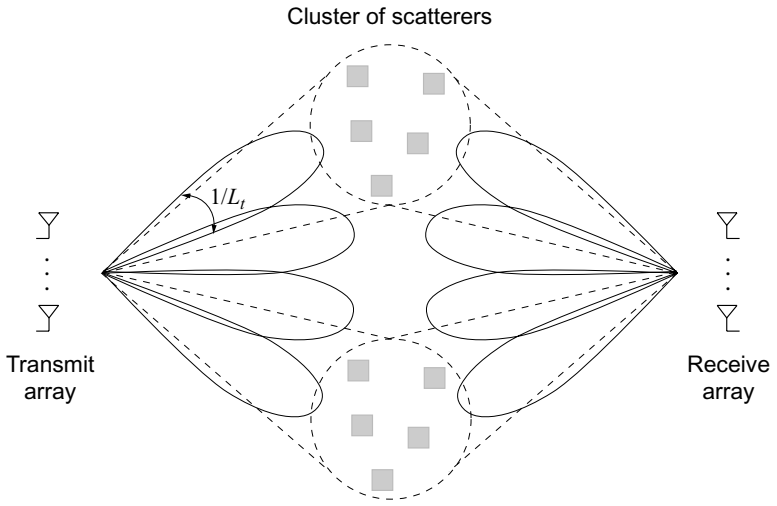

Figure 22: Illustrates the number of spatial multiplexed channels in an environment where the scattering clusters are far apart. Note that the beams plotted are over-simplified to ease explanation and do not reflect the actual $\Xi_{t,m}(\cdot)$ and $\Xi_{r,n}(\cdot)$.

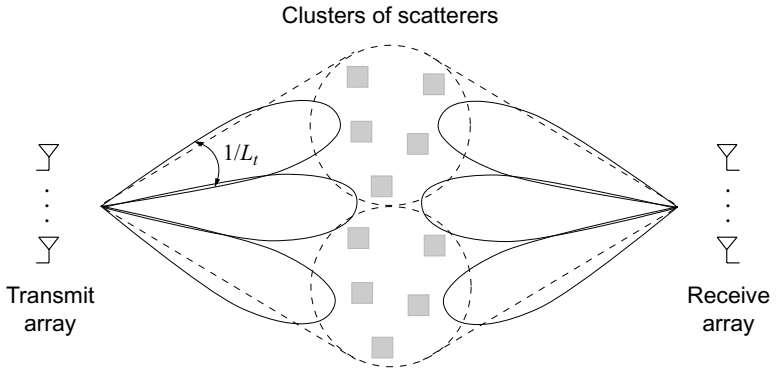

Figure 23: Illustrates the number of spatial multiplexed channels in an environment where the scattering clusters are adjacent to each other.

bandwidth, $|\Omega_{t,1}| = |\Omega_{t,2}| = 0.3$ but different angular separation[8]. In the first scenario, the clusters are the farthest apart. Fig. 21(a) shows that there are two strong singular values and two weak ones. Each cluster contributes a strong one. Furthermore, since $|\Omega_{t,m}| > 1/L_t$ and the transmit cluster separation is much greater than $1/L_t$, each cluster contributes an additional weaker one, as pictured in Fig. 22. This continues to apply even when the respective cluster separations are comparable to $1/L_t$ as in the second scenario and plotted in Fig. 21(b). Finally, when the clusters are close to each other, there are 2 strong singular values and a weak one as plotted in Fig. 21(c) and 21(d). Now the antenna arrays cannot distinguish those two clusters and perceive them as a single large cluster, and therefore the number of significant singular values can be approximated by $\lceil L_t|\Omega_t| \rceil$ which coincides with the result in the large-array regime. Fig. 23 gives a pictorial description. Two points are summarized:

- The disjointness among scattering clusters introduces more spreading in the distribution of singular values, and provides more viable transmission modes.
- The closeness between scattering clusters hinders the antenna arrays to separate them, and leads to the merging of scattering clusters. When the separation between any two clusters is less than the angular resolution of the antenna array, they would be merged as a single cluster.

Denote the angular intervals after merging as $\tilde{\Omega}_{t,i}$ and $\tilde{\Omega}_{r,i}$, and the respective number of them as $\tilde{M}_t$ and $\tilde{M}_r$. Based on the above two observations, the maximum multiplexing gain is approximated by

$$\sum_{i=1}^{\tilde{M}_t} \min\Big\{ \lceil L_t|\tilde{\Omega}_{t,i}| \rceil, \lceil L_r|\tilde{\Omega}_{r,i}| \rceil \Big\} \tag{92}$$

in both specular and single-bounce diffuse channels, and

$$\min\Big\{ \sum_{i=1}^{\tilde{M}_t} \lceil L_t|\tilde{\Omega}_{t,i}| \rceil, \sum_{i=1}^{\tilde{M}_r} \lceil L_t|\tilde{\Omega}_{r,i}| \rceil \Big\} \tag{93}$$

in the multi-bounce diffuse channel. Furthermore, the result in the multi-bounce diffuse channel is lower bounded by its large-array-regime counterpart as

$$\min\Big\{ \sum_{i=1}^{\tilde{M}_t} \lceil L_t|\tilde{\Omega}_{t,i}| \rceil, \sum_{i=1}^{\tilde{M}_r} \lceil L_t|\tilde{\Omega}_{r,i}| \rceil \Big\} \geq \min\big\{ L_t|\Omega_t|, L_r|\Omega_r| \big\} \tag{94}$$

The last paragraph of Section 5.4 brings out that there is an addition of

$$\frac{1}{c\pi^2} M_t \ln(2\pi L_t|\Omega_t|) \ln \mathsf{SNR}_\mathsf{r}$$

[8]The scenario is equivalent to transmit/receive arrays of length 24 cm at 5 GHz and an average cluster angle of 27°.

spatial degrees of freedom at high SNR where c equals 4 for specular channels, and is in between 2 and 4 for multi-bounce diffuse channels. These additional degrees of freedom increase with SNR, and are more apparent at the finite-array regime as the distribution of singular values is less abrupt. As pointed out, there is an infinite number of non-zero singular values. Whether these singular values corresponding to the spatial degrees of freedom depends on the SNR. At high SNR, small singular values that are once ignored are possible to contribute to the spatial degrees of freedom.

Fig. 24 plots the expected mutual information and the corresponding expected number of spatial channels in a multi-bounce diffuse channel with 3 randomly placed scattering clusters each of angle 30°, and array length of 2 and 4. Three power allocation schemes are investigated. The first scheme is guided by the result in the large-array regime where equal power is poured over the first $\lceil L_t|\Omega_t|\rceil$ spatial channels. The expected mutual information is given by

$$I_1 = \mathsf{E}_{\Omega_t,\mathbf{H}_w}\left[\log\det\Big(\mathbf{I} + \frac{\mathsf{SNR_r}}{\lceil L_t|\Omega_t|\rceil}\,\mathbf{H}_w\boldsymbol{\Sigma}_t^2\mathbf{H}_w^\dagger\boldsymbol{\Sigma}_t^2\Big)\right] \tag{95}$$

where $\mathbf{H}_w$ is a square matrix of dimension $\lceil L_t|\Omega_t|\rceil$. The second scheme is guided by (93) where equal power is poured over the first $\sum_{i=1}^{\tilde{M}_t}\lceil L_t|\tilde{\Omega}_{t,i}|\rceil$ ($\geq \lceil L_t|\Omega_t|\rceil$) spatial channels. The expected mutual information is given by

$$I_2 = \mathsf{E}_{\Omega_t,\mathbf{H}_w}\left[\log\det\Big(\mathbf{I} + \frac{\mathsf{SNR_r}}{\sum_{i=1}^{\tilde{M}_t}\lceil L_t|\tilde{\Omega}_{t,i}|\rceil}\,\mathbf{H}_w\boldsymbol{\Sigma}_t^2\mathbf{H}_w^\dagger\boldsymbol{\Sigma}_t^2\Big)\right] \tag{96}$$

where $\mathbf{H}_w$ is now of dimension $\sum_{i=1}^{\tilde{M}_t}\lceil L_t|\tilde{\Omega}_{t,i}|\rceil$. In the third scheme, waterfalling is performed over the singular values $\sigma_{t,m}$. This determines the number of spatial channels and the amount of power poured over them. The expected mutual information is given by

$$I_3 = \mathsf{E}_{\Omega_t,\mathbf{H}_w}\Big[\log\det\big(\mathbf{I} + \boldsymbol{\Sigma}_t\mathbf{H}_w\boldsymbol{\Sigma}_t\mathbf{K}\boldsymbol{\Sigma}_t\mathbf{H}_w^\dagger\boldsymbol{\Sigma}_t\big)\Big] \tag{97}$$

where $\mathbf{K}$ is a diagonal matrix,

$$K_{ii} = (\mu - \sigma_{t,i}^{-2})^+$$

and μ satisfies

$$\sum_i(\mu - \sigma_{t,i}^{-2})^+ = \mathsf{SNR_r}$$

Now, the dimension of $\mathbf{H}_w$ is the number of non-zero K_{ii}. Finally, the upper bound shown in the graphs is the ergodic capacity with full channel state information at both transmitter and receiver. From the graphs, two points are observed:

- At moderate SNR (up to 30 dB), the proposed approximation in (93) for the finite-array regime closely tracks the upper bound. The expected numbers of spatial channels guided by it are close to 4 for $L_t = 2$ and 6 for $L_t = 4$ wherease those guided by

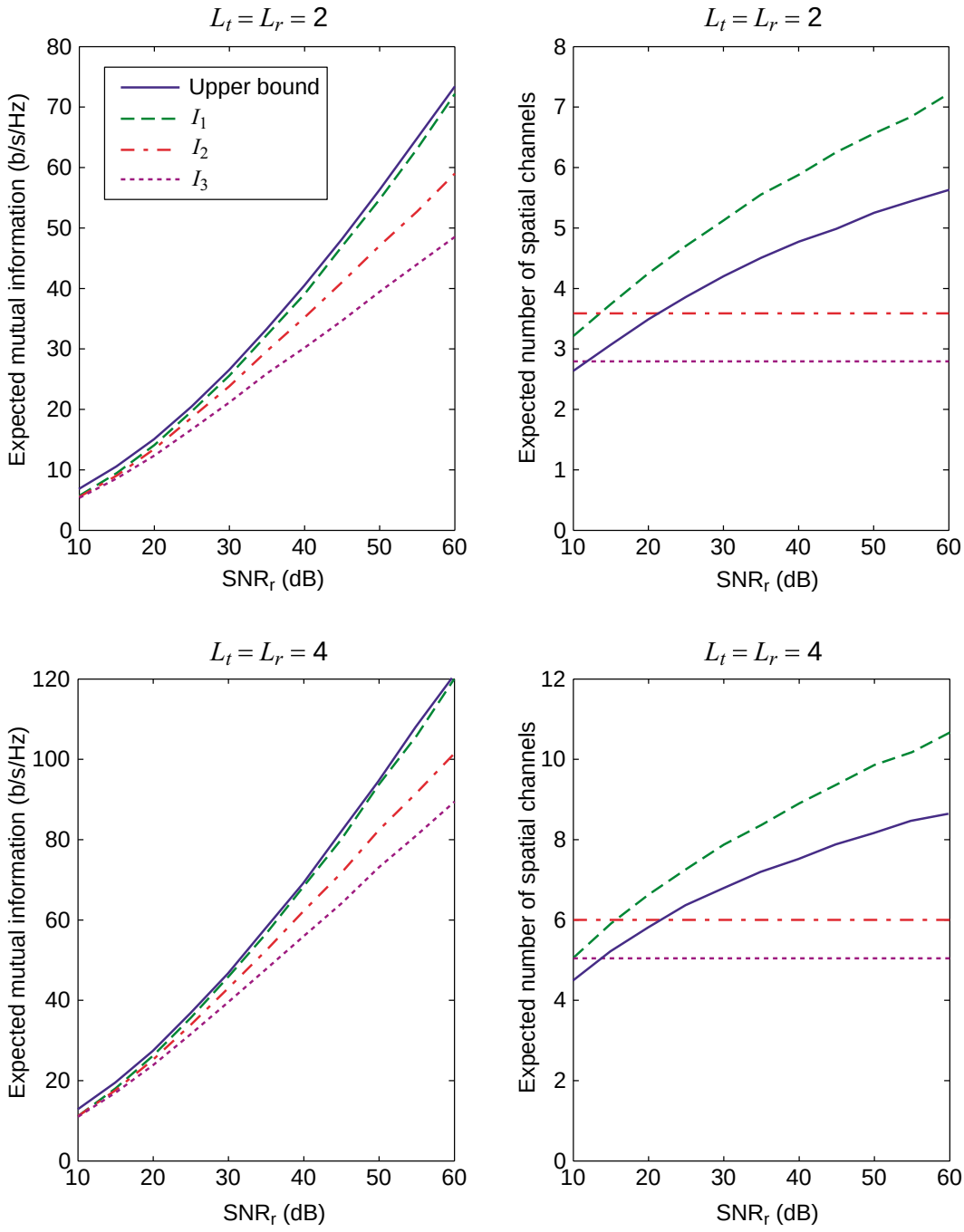

Figure 24: Plots the expected mutual information and the corresponding expected number of spatial channels using three different power allocation schemes.

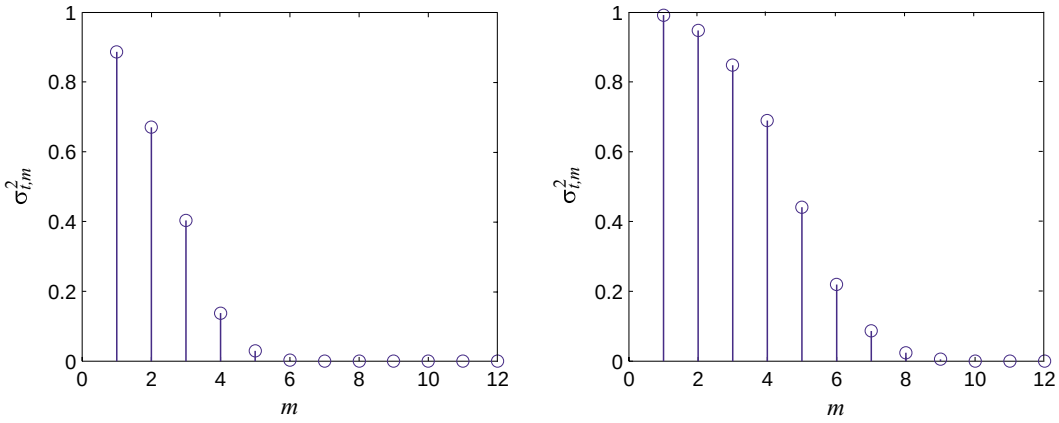

Figure 25: Plots the distribution of $\sigma^2_{t,m}$ for (left) $L_t = 2$ and (right) $L_t = 4$.

the result of the large-array regime are 3 and 5 respectively. Fig. 25 plots the distribution of $\sigma^2_{t,m}$. From which we notice that the approximations of 3 significant singular values for $L_t = 2$ and 5 for $L_t = 4$ are too conservative. The proposed approximation for the finite-array regime provides a better match and therefore the corresponding expected mutual information is in close proximity to the upper bound.

- At high SNR (above 30 dB), the proposed approximation cannot track the upper bound and the discrepancy increases with SNR. The scheme with waterfilling over $\sigma_{t,m}$, however, continues to follow the upper bound closely. Note that the expected number of spatial channels in the waterfilling scheme is greater than $2L_t$. This reveals that *a higher throughout is supported by packing more antennas beyond the well-established half-wavelength antenna spacing criterion.*

Now we attempt to elucidate the second observation from electromagnetic theory. In principle, any radiating system can generate infinite number of transmission modes implying that a small array can generate the same radiation pattern as a large array. However, in order to generate the same radiation pattern, one needs to pack the same amount of moving charges in both arrays. More power is needed to keep the charges in the small array than in the large array[9]. Therefore, a higher SNR is required by a small array to generate comparable number of spatial channels as a large array. Consequently, the number of spatial channels should depend on the SNR as well.

[9]Since the amount of moving charges is the same, the small array has a higher current density than the large array. A higher current density, in turn, builds up a larger radiation reaction, the self force to hold charges together. Hence, the small array will have a poorer radiation efficiency because most of its energy is consumed to hold the charges in a small volume instead of radiating out.

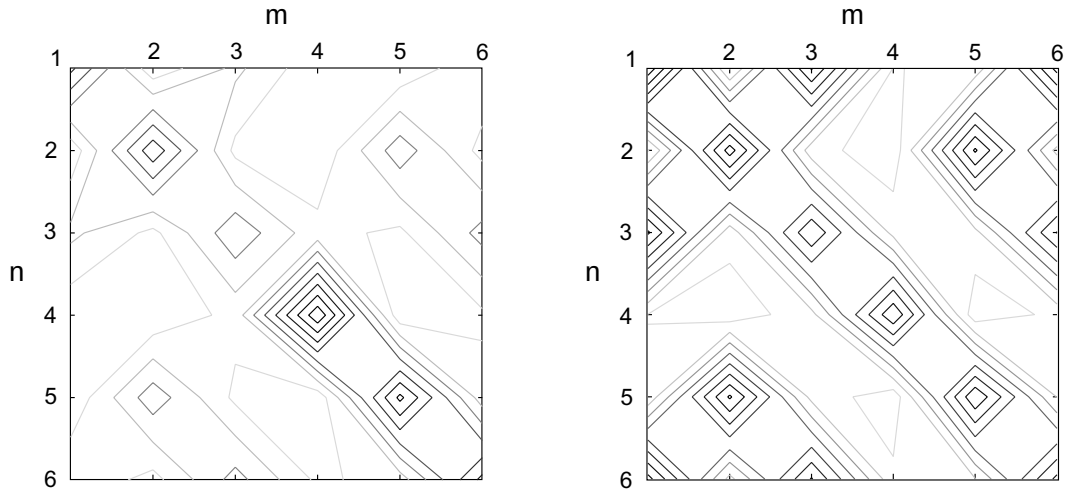

Figure 26: Plots the contour of the variance of the channel matrix $\mathbf{H}$ for (left) specular and (right) single-bounce diffuse channels with $\Theta_t = [25°, 55°] \cup [80°, 110°] \cup [145°, 175°]$ and $L_t = 4$. The angular resolution of the model is 0.01 radian, compared to the $1/L_t = 0.25$ radian of antenna arrays. In the specular channel, the phase lag of physical paths are uniformly distributed and independent of each other.

6.2 Randomness of H

The finite angular resolution of antenna arrays in this regime brings in two issues:

- In specular channels, physical paths can no longer be resolved individually but are perceived as aggregations. This introduces randomness on the diagonal elements of the channel matrix.
- The basis functions $\eta^*_{r,n}(\beta)\eta_{t,m}(\alpha)$ spread more over the entire $\Omega_r \times \Omega_t$. This introduces randomness on the off-diagonal elements of specular channels and the off-block-diagonal submatrices of single-bounce diffuse channels. The variances would be less than the respective diagonal elements and block-diagonal submatrices. Furthermore, these random variables would be correlated to the respective diagonal counterparts.

The multi-bounce diffuse channels, however, are the same regardless of the size of antenna arrays due to the property explained in (65).

Fig. 26 plots the variance of the channel matrices in an environment with 3 scattering clusters at $\Theta_t = [25°, 55°] \cup [80°, 110°] \cup [145°, 175°]$ and $L_t = 4$. The dimension of the matrices is given by (93) and equals to 6 in which $\lceil L_t|\Omega_{t,1}|\rceil = 2$, $\lceil L_t|\Omega_{t,2}|\rceil = 3$, and $\lceil L_t|\Omega_{t,3}|\rceil = 1$. In the specular channel, the variance of diagonal elements is clustered around three regions. The variance of off-diagonal elements is small and mostly negligible.

In the single-bounce diffuse channels, the variances are concentrated along the diagonal as well as the left lower corner and the right upper corner. Those two corners correspond to projections onto the most optimal radiation patterns and reception patterns respectively.

Apparently, the finite angular resolution of antenna arrays would introduce more randomness on the channel matrix. This would make a specular channel more like a single-bounce diffuse channel and a single-bounce diffuse channel more like a multi-bounce diffuse channel. In the extreme case, when the angular resolution is omni-directional as in the small-array regime, all three channels have the same randomness.

7 A Two-Stage Transceiver Architecture

The impact of scattering has two spatial scales. In the coarse scale, the total widths of cluster intervals, $|\Omega_t|$ and $|\Omega_r|$, determine the dimension of the channel matrix while the detail location of those intervals, Ω_t and Ω_r, defines the set of basis functions that gives the most compact view of the channel. In the fine scale, the underlying scattering mechanism affects the scattering response within $\Omega_r \times \Omega_t$ which in turn affects the magnitude and randomness of the channel matrix. This hierarchical understanding of scattering suggests a two-stage transceiver architecture for the channel estimation of multiple-antenna systems.

The first stage accounts for the coarse-scale scattering and estimates the amount of channel resources along the spatial dimension supported by the physical environment. It involves the following sequence of operations at the transceiver:

- The receiver estimates Ω_t and Ω_r, and sends the estimated Ω_t back to the transmitter.
- Both the transmitter and the receiver then compute the set of optimal radiation patterns and reception patterns respectively as well as the available number of spatial degrees of freedom.

The second stage accounts for the fine-scale scattering and zooms in on the available channel resources along the spatial dimension. It involves the following operations:

- The receiver estimates the channel matrix viewed over the basis determined at the first stage, and learns the randomness of the channel matrix.
- The receiver then updates the transmitter about this randomness. Based on which the transmitter adjusts the space-time coding schemes used.

Fig. 27 shows the block diagram of the transceiver architecture.

The feedback involved is little. In the first stage, only the cluster boundaries are sent back, that is, $2M_t$ real numbers. In the second stage, as little information as whether the channel is specular, single-bounce diffuse, or multi-bounce diffuse, suffices. For wideband

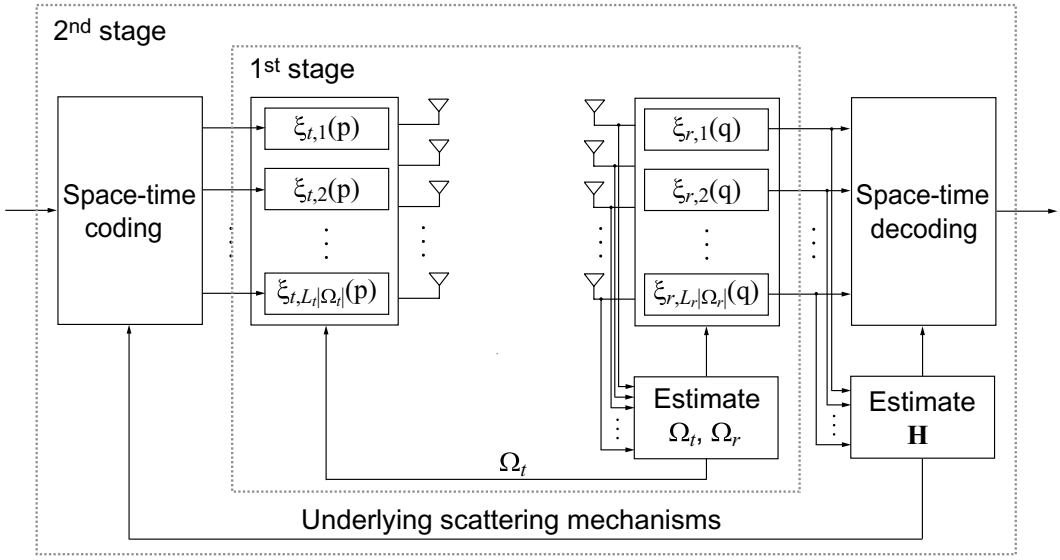

Figure 27: Block diagram of the two-stage transceiver architecture for the channel estimation of multiple-antenna systems.

systems, the cluster boundaries and the underlying scattering mechanism are expected to be more or less the same over the entire bandwidth. When multicarrier transmission is used, the amount of feedback per subcarrier is negligible. In addition, the channel estimation at the second stage is undertaking over an optimal basis, the complexity is therefore kept to the minimum.

8 Conclusions

In this paper, we use a continuous-array model, and introduce a two-step approach to model the scattering condition of channels in an array-independent but manageable description of physical environments. Based on this model, we investigate the impact of scattering on the spatial multiplexing gain, the diversity gain, as well as the trade-off among spatial multiplexing, diversity, and propagation range. The results help assess the available channel resources from the scattering nature of physical environments. Whether a transceiver can fully utilize these available resources, depends on the sophistication of the transceiver. Obviously, the denser the antennas is, the closer is the performance approaching the optimum. Of course, when antennas are putting too close to each other, there is mutual coupling among them. In this case, we cannot ignore the element responses in (8). However, the distributions of the singular values $\sigma_{t,m}$ and $\sigma_{r,n}$ would reveal the optimal number of antennas. Beyond which there will be diminishing return on performances.

Furthermore, we introduce a more direct approach to capture the propagation range

into the performance studies. To reinforce this approach, Hypothesis 4.1 needs to be tested by experiments. Finally, we use the outage formulation proposed in [25] to bring out the effect of different scattering mechanisms on the diversity benefit of multiple-antenna systems. Other formulations such as using the variance of mutual information [29] can be substituted to capture the essence of underlying scattering mechanisms.

A Proof of Lemma 5.2

First, we solve μ:

$$\begin{aligned}\mathsf{SNR_t} &= \int \Big(\mu - \frac{1}{x^2}\Big)^+ dG_t(x) + o\big(\ln(L_t|\Omega_t|)\big) \\ &= (\mu-1)L_t|\Omega_t| + \frac{1}{\pi^2} M_t \ln(2\pi L_t|\Omega_t|)\Big[(\mu-1)\ln(\sqrt{\mu}-1) - \frac{\mu}{2} \\ &\quad - \sqrt{\mu} + \frac{1}{2(1-\varepsilon_t)^2} + \frac{1}{1-\varepsilon_t}\Big] + o\big(\ln(L_t|\Omega_t|)\big) \\ &= (\mu-1)L_t|\Omega_t| + o\big(\ln(L_t|\Omega_t|)\big)\end{aligned}$$

implying

$$\mu = 1 + \frac{\mathsf{SNR_t}}{L_t|\Omega_t|} + o(1)$$

as $L_t|\Omega_t| \to \infty$. Then, C_{SP} can be written as

$$\begin{aligned}C_{SP} &= \int_{1/\sqrt{\mu}}^{1-\varepsilon_t} \log(x^2\mu)\, dG_t(x) + o\big(\ln(L_t|\Omega_t|)\big) \\ &= \log\mu \int_{1/\sqrt{\mu}}^{1-\varepsilon} dG_t(x) + 2\int_{1/\sqrt{\mu}}^{1-\varepsilon} \log x\, dG_t(x) + o\big(\ln(L_t|\Omega_t|)\big)\end{aligned}$$

The integral in the first term is

$$L_t|\Omega_t| + \frac{1}{\pi^2} M_t \ln(2\pi L_t|\Omega_t|)\ln(\sqrt{\mu}-1)$$

and the integral in the second term is

$$\begin{aligned}&\frac{1}{\pi^2\ln 2} M_t \ln(2\pi L_t|\Omega_t|) \int_{1/\sqrt{\mu}}^{1-\varepsilon_t} \frac{\ln x}{x} + \frac{\ln x}{1-x}\, dx \\ =&\frac{1}{\pi^2\ln 2} M_t \ln(2\pi L_t|\Omega_t|)\Big[\frac{1}{2}\ln^2(1-\varepsilon_t) - \frac{1}{8}\ln^2\mu + \mathrm{Li}_2(\varepsilon_t) - \mathrm{Li}_2(1-1/\sqrt{\mu})\Big]\end{aligned}$$

As ε_t tends to 0 as $L_t|\Omega_t|$ tends to ∞, the capacity can be written as

$$C_{SP} = \Big[L_t|\Omega_t| + M_t \ln(2\pi L_t|\Omega_t|) f_1(\mathsf{SNR_t})\Big]\log\mu + o\big(\ln(L_t|\Omega_t|)\big)$$

as $L_t|\Omega_t| \to \infty$, where

$$\begin{aligned} f_1(\mathsf{SNR_t}) &= \frac{1}{\pi^2}\Big[\ln(\sqrt{\mu}-1) - \frac{1}{4}\ln\mu - \frac{2}{\ln 2}\,\mathrm{Li}_2(1-1/\sqrt{\mu})/\log\mu\Big] \\ &= \frac{1}{4\pi^2}\ln\frac{\mathsf{SNR_t}}{L_t|\Omega_t|} + o(\ln \mathsf{SNR_t}) \end{aligned}$$

as $\mathsf{SNR_t} \to \infty$.

B Proof of Lemma 5.3

The $F_{t,\epsilon}(x)$ can be expressed as

$$F_{t,\epsilon}(x) = \frac{M_t \ln(2\pi L_t|\Omega_t|)}{\pi^2 \bar{G}_t(\epsilon)}\Big(\ln\frac{1-\epsilon}{\epsilon} - \ln\frac{1-x}{x}\Big) + o\Big(\frac{\ln(L_t|\Omega_t|)}{L_t|\Omega_t|}\Big)$$

Now, we have

$$\int_\epsilon^1 \log x\, dF_{t,\epsilon}(x) = -\frac{M_t \ln(2\pi L_t|\Omega_t|)}{2\pi^2 \bar{G}_t(\epsilon)\ln 2}\big[\ln^2\epsilon + 2\,\mathrm{Li}_2(1-\epsilon)\big] + o\Big(\frac{\ln(L_t|\Omega_t|)}{L_t|\Omega_t|}\Big)$$

which yields

$$\begin{aligned} C_{MD} \gtrsim L_t|\Omega_t|\log\frac{\mathsf{SNR_t}}{l^{\nu-1}e} + \frac{1}{\pi^2}M_t\ln(2\pi L_t|\Omega_t|)\Big[\log\frac{\mathsf{SNR_t}}{l^{\nu-1}e}\ln\frac{1-\epsilon}{\epsilon} \\ - \log\epsilon\ln\epsilon - \frac{2}{\ln 2}\,\mathrm{Li}_2(1-\epsilon)\Big] + o\big(\ln(L_t|\Omega_t|)\big) \end{aligned}$$

as $L_t|\Omega_t| \to \infty$, for all $\epsilon \in (0,1)$. Now, we pick

$$\epsilon = \Big(\sqrt{\frac{\mathsf{SNR_t}}{l^{\nu-1}e}}\,\Big)^{-1} \tag{98}$$

and complete the proof.

C Proof of Lemma 5.4

Applying Lemma 5.1, we obtain

$$\begin{aligned} C_{MD} &\le \int_0^{1-\varepsilon_t} \log\Big(1+\frac{\mathsf{SNR_t}}{l^{\nu-1}}x\Big)\,dG(x) + o\big(\ln(L_t|\Omega_t|)\big) \\ &= \frac{1}{\pi^2}M_t\ln(2\pi L_t|\Omega_t|)\int_0^{1-\varepsilon_t}\frac{1}{x(1-x)}\log\Big(1+\frac{\mathsf{SNR_t}}{l^{\nu-1}}x\Big)\,dx + o\big(\ln(L_t|\Omega_t|)\big) \\ &= \frac{1}{\pi^2\ln 2}M_t\ln(2\pi L_t|\Omega_t|)\int_0^{1-\varepsilon_t}\frac{1}{x}\ln\Big(1+\frac{\mathsf{SNR_t}}{l^{\nu-1}}x\Big) + \frac{1}{1-x}\ln\Big(1+\frac{\mathsf{SNR_t}}{l^{\nu-1}}x\Big)\,dx \\ &\quad + o\big(\ln(L_t|\Omega_t|)\big) \end{aligned}$$

The first integral is

$$\int_0^{1-\varepsilon_t} \frac{1}{x} \ln\Big(1+\frac{\mathsf{SNR_t}}{l^{\nu-1}}x\Big)\,dx = -\operatorname{Li}_2\Big(-\frac{\mathsf{SNR_t}}{l^{\nu-1}}(1-\varepsilon_t)\Big)$$

and the second integral is

$$\begin{aligned}
&\int_0^{1-\varepsilon_t} \frac{1}{1-x} \ln\Big(1+\frac{\mathsf{SNR_t}}{l^{\nu-1}}x\Big)\,dx \\
=&\frac{\pi^2 L_t|\Omega_t|}{M_t \ln(2\pi L_t|\Omega_t|)} \ln\Big(1+\frac{\mathsf{SNR_t}}{l^{\nu-1}}(1-\varepsilon_t)\Big) - \ln\Big(1+\frac{\mathsf{SNR_t}}{l^{\nu-1}}(1-\varepsilon_t)\Big) \ln\frac{\mathsf{SNR_t}/l^{\nu-1}(1-\varepsilon_t)}{1+\mathsf{SNR_t}/l^{\nu-1}} \\
&- \operatorname{Li}_2\Big(\frac{1+\mathsf{SNR_t}/l^{\nu-1}(1-\varepsilon_t)}{1+\mathsf{SNR_t}/l^{\nu-1}}\Big) + \operatorname{Li}_2\Big(\frac{1}{1+\mathsf{SNR_t}/l^{\nu-1}}\Big)
\end{aligned}$$

As ε_t approaches 0 for large $L_t|\Omega_t|$ and

$$\lim_{\mathsf{SNR_t}\to\infty} \frac{-\operatorname{Li}_2(-\mathsf{SNR_t}/l^{\nu-1})}{\ln^2(\mathsf{SNR_t}/l^{\nu-1})} = \frac{1}{2}$$

the upper-bound can be expressed as

$$C_{MD} \le \Big[L_t|\Omega_t| + M_t \ln(2\pi L_t|\Omega_t|) f_3(\mathsf{SNR_t})\Big] \log\Big(1+\frac{\mathsf{SNR_t}}{l^{\nu-1}}\Big) + o\big(\ln(L_t|\Omega_t|)\big)$$

as $L_t|\Omega_t| \to \infty$, where

$$f_3(\mathsf{SNR_t}) = \frac{1}{2\pi^2} \ln\frac{\mathsf{SNR_t}}{l^{\nu-1}} + o(\ln \mathsf{SNR_t})$$

as $\mathsf{SNR_t} \to \infty$.

D Proof of Theorem 5.6

The channel matrix for the single-bounce diffuse channel is block diagonal and each diagonal sub-block is an i.i.d. fading channel by itself. Suppose $d_i(r)$ satisfy

$$\lim_{\mathsf{SNR_r}\to\infty} \frac{\log P\big[\det(\mathbf{I}+\frac{\mathsf{SNR_r}}{L_t|\Omega_{t,i}|}\mathbf{H}_i^\dagger\mathbf{H}_i) < \mathsf{SNR_r}^r\big]}{\log \mathsf{SNR_r}} = -d_i(r)$$

for $i = 1, \cdots, M_t$. The next lemma gives $d_{SD}(r)$ in terms of $d_i(r)$'s.

Lemma D.1. *The trade-off curve $d_{SD}(r)$ is*

$$d_{SD}(r) = d_1(r) \oplus d_2(r) \oplus \cdots \oplus d_{M_t}(r)$$

Proof. We follow the notation in [25] and use the symbol $\doteq$ to denote

$$\lim_{\mathsf{SNR_r}\to\infty} \frac{\log g(\mathsf{SNR_r})}{\log_2 \mathsf{SNR_r}} = b \iff g(\mathsf{SNR_r}) \doteq \mathsf{SNR_r}^b$$

Then, $d_i(r)$ satisfies

$$P\big[\det(\mathbf{I}+\mathsf{SNR_r}\mathbf{H}_i^\dagger\mathbf{H}_i)<\mathsf{SNR_r}^r\big]\doteq\mathsf{SNR_r}^{-d_i(r)}$$

for $i=1,\cdots,M_t$. Let $\mathsf{SNR_r}^{\theta_i}=\det(\mathbf{I}+\mathsf{SNR_r}\mathbf{H}_i^\dagger\mathbf{H}_i)$ for $i=1,\cdots,M_t$. The cdf of θ_i is

$$F_{\theta_i}(\theta)=P(\theta_i<\theta)\doteq\mathsf{SNR_r}^{-d_i(\theta)}$$

and thus, its pdf is

$$f_{\theta_i}(\theta)\doteq\frac{d}{d\theta}\,\mathsf{SNR_r}^{-d_i(\theta)}=\mathsf{SNR_r}^{-d_i(\theta)}\,\ln\mathsf{SNR_r}\,\frac{d}{d\theta}\,d_i(\theta)\doteq\mathsf{SNR_r}^{-d_i(\theta)}$$

ignoring the sign. Since the sub-blocks are independent, so

$$\begin{aligned}
&P\bigg[\prod_{i=1}^{M_t}\det\Big(\mathbf{I}+\frac{\mathsf{SNR_r}}{L_t|\Omega_{t,i}|}\mathbf{H}_i^\dagger\mathbf{H}_i\Big)<\mathsf{SNR_r}^r\bigg]\\
\doteq\;&P\bigg[\prod_{i=1}^{M_t}\det(\mathbf{I}+\mathsf{SNR_r}\mathbf{H}_i^\dagger\mathbf{H}_i)<\mathsf{SNR_r}^r\bigg]\\
=\;&P\Big(\sum_{i=1}^{M_t}\theta_i<r\Big)\\
=\;&(F_{\theta_1}*f_{\theta_2}*\cdots*f_{\theta_{M_t}})(r)\\
=\;&\int_0^r\int_0^{\theta_2}\cdots\int_0^{\theta_{M_t-1}}F_{\theta_1}(r-\theta_2)f_{\theta_2}(\theta_2-\theta_3)\cdots f_{\theta_{M_t}}(\theta_{M_t})\,d\theta_{M_t}\cdots d\theta_3\,d\theta_2\\
=\;&\int_0^r\int_0^{\theta_2}\cdots\int_0^{\theta_{M_t-1}}\mathsf{SNR_r}^{-\left[d_1(m-\theta_2)+d_2(\theta_2-\theta_3)+\cdots+d_{M_t}(\theta_{M_t})\right]}\,d\theta_{M_t}\cdots d\theta_3\,d\theta_2\\
\doteq\;&\mathsf{SNR_r}^{-d_{SD}(r)}
\end{aligned}$$

where

$$d_{SD}(r)=\inf_{\substack{0\le\theta_2\le r\\0\le\theta_3\le\theta_2\\\vdots\\0\le\theta_{M_t}\le\theta_{M_t-1}}}\big[d_1(r-\theta_2)+d_2(\theta_2-\theta_3)+\cdots+d_{M_t-1}(\theta_{M_t-1}-\theta_{M_t})+d_{M_t}(\theta_{M_t})\big]$$

Therefore, $d_{SD}(r)$ can be expressed as a series of min-plus convolution

$$d_{SD}(r)=(d_1\oplus d_2\oplus\cdots\oplus d_{M_t})(r)$$

□

Now, $d_i(r)$'s are decreasing and piecewise linear with end-points at $(0,L_tL_r|\Omega_{t,i}||\Omega_{r,i}|)$ and $(\min\{L_t|\Omega_{t,i}|,L_r|\Omega_{r,i}|\},0)$. Consequently, $d_{SD}(r)$ has the following property.

Lemma D.2. *The trade-off curve $d_{SD}(r)$ is obtained by putting end-to-end the different linear pieces in $d_i(r)$'s, sorted by increasing slopes (or equivalently, decreasing negative slopes).*

Proof. It is sufficient to show that the statement holds for $M_t = 2$. Let $\tilde{d}(r)$ denote the claimed curve, and the slopes of $d_1(r)$ and $d_2(r)$ be $0 \geq s_1 \geq s_2 \geq \cdots \geq s_L$, with the corresponding length of projection onto the horizontal axis being $\alpha_1, \alpha_2, \cdots, \alpha_L$ where $L = \min\{L_t|\Omega_{t,1}|, L_r|\Omega_{r,1}|\} + \min\{L_t|\Omega_{t,2}|, L_r|\Omega_{r,2}|\}$. Furthermore, let $\mathcal{S}_n$ be the set of index of slopes belonging to $d_n(r)$, for $n = 1, 2$. Then, for $r \in \left[L - \sum_{i=1}^{l} \alpha_i, L - \sum_{i=1}^{l-1} \alpha_i\right]$, the claimed curve is

$$\tilde{d}(r) = -\sum_{i=1}^{l-1} s_i \alpha_i - s_l \left(L - \sum_{i=1}^{l-1} \alpha_i - r \right)$$

Assume without loss of generality, $l \in \mathcal{S}_2$. Now we will show that when $r = L - \sum_{i=1}^{l-1} \alpha_i - \Delta$ for some $\Delta \in [0, \alpha_l)$,

$$d_1(u) + d_2(r-u) \geq d_1(a) + d_2(b), \quad \forall u \in [0, r] \tag{99}$$

where

$$a = \min\{L_t|\Omega_{t,1}|, L_r|\Omega_{r,1}|\} - \sum_{\substack{1 \leq i \leq l-1 \\ i \in \mathcal{S}_1}} \alpha_i$$

$$b = \min\{L_t|\Omega_{t,2}|, L_r|\Omega_{r,2}|\} - \sum_{\substack{1 \leq i \leq l-1 \\ i \in \mathcal{S}_2}} \alpha_i - \Delta$$

1° $u \leq a$

As $d_n(r)$'s are decreasing and piecewise linear,

$$d_1(u) - d_1(a) \geq -s_l(a - u)$$

Note that $a + b = r$ and hence $r - u \geq b$. Thus,

$$d_2(b) - d_2(r-u) \leq -s_l(r - u - b) = -s_l(a - u)$$

Combining both inequalities gives the desired result.

2° $u > a$

Similarly, we have

$$d_1(a) - d_1(u) \leq -s_l(u - a)$$

$$d_2(r-u) - d_2(b) \geq -s_l(b - r + u) = -s_l(u - a)$$

Combining them gives the desired result as well.

Back to (99), it can be expressed as

$$\begin{aligned} d_1(u) + d_2(r-u) &\geq d_1(a) + d_2(b) \\ &= -\sum_{\substack{1\leq i\leq l-1 \\ i\in\mathcal{S}_1}} s_i\alpha_i - \sum_{\substack{1\leq i\leq l-1 \\ i\in\mathcal{S}_2}} s_i\alpha_i - s_l\Delta \\ &= -\sum_{i=1}^{l-1} s_i\alpha_i - s_l\left(L - \sum_{i=1}^{l-1}\alpha_i - r\right) \\ &= \tilde{d}(r) \end{aligned}$$

for all $u \in [0, r]$. Since $d_{SD}(r)$ is the infimum of the sum on the left over all u from 0 to r, so it coincides with the claimed curve on the right. □

References

[1] J. Salz and J. H. Winters, "Effect of fading correlation on adaptive arrays in digital mobile radio," *IEEE Trans. Veh. Technol.*, vol. 43, no. 4, pp. 1049–57, Nov. 1994.

[2] G. G. Raleigh and J. M. Cioffi, "Spatio-temporal coding for wireless communication," *IEEE Trans. Commun.*, vol. 46, no. 3, pp. 357–66, Mar. 1998.

[3] D. S. Shiu, G. J. Foschini, M. J. Gans, and J. M. Kahn, "Fading correlation and its effect on the capacity of multielement antenna systems," *IEEE Trans. Commun.*, vol. 48, pp. 502–13, Mar. 2000.

[4] H. Bölcskei, D. Gesbert, and A. J. Paulraj, "On the capacity of OFDM-based spatial multiplexing systems," *IEEE Trans. Commun.*, vol. 50, pp. 225–34, Feb. 2002.

[5] C. N. Chuah, D. Tse, J. M. Kahn, and R. A. Valenzuela, "Capacity scaling in MIMO wireless systems under correlated fading," *IEEE Trans. Inform. Theory*, vol. 48, no. 3, pp. 637–50, Mar. 2002.

[6] R. R. Müller, "A random matrix model of communication via antenna arrays," *IEEE Trans. Inform. Theory*, vol. 48, no. 9, pp. 2495–06, Sept. 2002.

[7] A. M. Sayeed, "Deconstructing multi-antenna fading channels," *IEEE Trans. Signal Process.*, vol. 50, pp. 2563–79, Oct. 2002.

[8] D. Gesbert, T. Ekman, and N. Christophersen, "Capacity limits of dense palm-sized MIMO arrays," in *Proc. IEEE GLOBECOM*, vol. 2, Taipei, Taiwan, Nov. 2002, pp. 17–21.

[9] T. S. Pollock, T. D. Abhayapala, and R. A. Kennedy, "Antenna saturation effects on MIMO capacity," in *Proc. IEEE Int. Conf. Communications*, vol. 3, Anchorage, AK, May 2003, pp. 2301–05.

[10] H. Özcelik and M. Herdin and W. Weichselberger and J. Wallace and E. Bonek, "Deficiencies of Kronecker MIMO radio channel model," *Electronics Letters*, vol. 39, no. 16, pp. 1209–10, Aug. 2003.

[11] M. Debbah and R. Müller, "Capacity complying MIMO channel models," in *Proc. Asilomar Conf. Signals, Systems and Computers*, vol. 2, Pacific Grove, CA, Nov. 2003, pp. 1815–19.

[12] J. W. Wallace and M. A. Jensen, "Intrinsic capacity of the MIMO wireless channel," in *Proc. VTC*, vol. 2, Vancouver, Canada, Sept. 2002, pp. 701–05.

[13] R. Heddergott and P. Truffer, "Statistical characteristics of indoor radio propagation in NLOS scenarios," Tech. Rep. COST 259 TD(00) 024, Valencia, Spain, Tech. Rep. COST 259, Jan. 2000.

[14] Q. H. Spencer *et al.*, "Modeling the statistical time and angle of arrival characteristics of an indoor multipath channel," *IEEE J. Select. Areas Commun.*, vol. 18, pp. 347–60, Mar. 2000.

[15] R. J.-M. Cramer, "An evaluation of ultra-wideband propagation channels," Ph.D. dissertation, University of Southern California, Dec. 2000.

[16] A. S. Y. Poon and M. Ho, "Indoor multiple-antenna channel characterization from 2 to 8 GHz," in *Proc. IEEE Int. Conf. Communications*, vol. 5, Anchorage, AK, May 2003, pp. 3519–23.

[17] A. S. Y. Poon, R. W. Brodersen, and D. N. C. Tse, "Degrees of freedom in multiple-antenna channels: a signal space approach," *IEEE Trans. Inform. Theory*, vol. 51, no. 2, Feb. 2005.

[18] J. D. Kraus and R. J. Marhefka, *Antennas*, 3rd ed. McGraw-Hill, 2001.

[19] T. S. Rappaport, *Wireless Communications: Principle and Practice*, 2nd ed. Prentice Hall PTR, 2002.

[20] S. Y. Seidel and T. S. Rappaport, "914 MHz path loss prediction models for indoor wireless communications in multifloored buildings," *IEEE Trans. Antennas Propagat.*, vol. 40, no. 2, pp. 207–17, Feb. 1992.

[21] J. B. Anderson, T. S. Rappaport, and S. Yoshida, "Propagation measurements and models for wireless communications channels," *IEEE Commun. Mag.*, vol. 33, no. 1, pp. 42–49, Jan. 1995.

[22] M. Steinbauer, A. F. Molisch, and E. Bonek, "The double-directional radio channel," *IEEE Antennas Propagat. Mag.*, vol. 43, no. 4, pp. 51–63, Aug. 2001.

[23] L. Tsang, J. A. Kong, and K. H. Ding, *Scattering of Electromagnetic Waves: Theories and Applications*. Wiley, 2000.

[24] R. G. Gallager, *Information Theory and Reliable Communication*. Wiley, 1968.

[25] L. Zheng and D. N. C. Tse, "Diversity and multiplexing: a fundamental tradeoff in multiple antenna channels," *IEEE Trans. Inform. Theory*, vol. 49, pp. 1073–96, May 2003.

[26] D. Slepian, "Some asymptotic expansions for prolate spheroidal wave functions," *J. of Mathematics and Physics*, vol. 44, pp. 99–140, 1965.

[27] V. L. Girko, *Theory of Random Determinants*. Norwell, MA: Kluwer, 1990.

[28] D. Gesbert, "Multipath: Curse or blessing? a system performance analysis of MIMO wireless systems," in *Proc. of Intl. Zurich Seminar on Commun.*, 2004, pp. 14–17.

[29] Ö. Oyman and R. U. Nabar and H. Bölcskei and A. J. Paulraj, "Characterizing the statistical properties of mutual information in MIMO channels," *IEEE Trans. Signal Process.*, vol. 51, no. 11, pp. 2784–95, Nov. 2003.